Draft version October 30, 2018
Preprint typeset using LaTeX style emulateapj v. 08/22/09

DETECTION OF A POPULATION OF CARBON-ENHANCED METAL-POOR STARS IN THE SCULPTOR DWARF SPHEROIDAL GALAXY*

Anirudh Chiti[1,2,*], Joshua D. Simon[3], Anna Frebel[1,2], Ian B. Thompson[3], Stephen A. Shectman[3], Mario Mateo[4], John I. Bailey, III[5], Jeffrey D. Crane[3], Matthew Walker[6]

Draft version October 30, 2018

ABSTRACT

The study of the chemical abundances of metal-poor stars in dwarf galaxies provides a venue to constrain paradigms of chemical enrichment and galaxy formation. Here we present metallicity and carbon abundance measurements of 100 stars in Sculptor from medium-resolution ($R \sim 2000$) spectra taken with the Magellan/Michigan Fiber System mounted on the Magellan-Clay 6.5m telescope at Las Campanas Observatory. We identify 24 extremely metal-poor star candidates ([Fe/H] < -3.0) and 21 carbon-enhanced metal-poor (CEMP) star candidates. Eight carbon-enhanced stars are classified with at least 2σ confidence and five are confirmed as such with follow-up $R \sim 6000$ observations using the Magellan Echellette Spectrograph on the Magellan-Baade 6.5m telescope. We measure a CEMP fraction of 36% for stars below [Fe/H] $= -3.0$, indicating that the prevalence of carbon-enhanced stars in Sculptor is similar to that of the halo ($\sim 43\%$) after excluding likely CEMP-s and CEMP-r/s stars from our sample. However, we do not detect that any CEMP stars are strongly enhanced in carbon ([C/Fe] > 1.0). The existence of a large number of CEMP stars both in the halo and in Sculptor suggests that some halo CEMP stars may have originated from accreted early analogs of dwarf galaxies.

Subject headings: galaxies: dwarf — galaxies: individual (Sculptor dSph) — galaxies: stellar content — stars: abundances — stars: carbon

1. INTRODUCTION

The oldest stars in the Milky Way contain trace amounts of elements heavier than helium (or "metals") and measurements of their relative chemical abundances provide key constraints on the early phases of chemical evolution (e.g. McWilliam 1997; Kirby et al. 2011), galaxy formation (e.g. Freeman & Bland-Hawthorn 2002), and the star-formation history (SFH) and initial mass function (IMF) of their birth environment (e.g. Bromm & Larson 2004). Studying metal-poor (MP) stars ([Fe/H] < -1.0, where [Fe/H] $= \log_{10}(N_{Fe}/N_H)_\star - \log_{10}(N_{Fe}/N_H)_\odot$) and in particular, extremely metal-poor (EMP) stars ([Fe/H] < -3.0) in the Milky Way's dwarf satellite galaxies effectively probes the aforementioned topics due to the simpler dynamical and chemical evolution histories of dwarf galaxy systems (see Tolstoy et al. 2009 for a complete review). Furthermore, dwarf galaxies have innate cosmological significance as they are hypothesized to be the surviving analogs of the potential building blocks of larger systems in hierarchical galaxy formation scenarios. Studying the most metal-poor stars in these systems is a promising avenue to explore this intriguing potential connection.

While the specific relationship between dwarf galaxies and their ancient analogs is not entirely understood, detailed abundance studies of the most metal-poor stars in ultra-faint dwarf galaxies and classical dwarf spheroidal (dSph) galaxies have shown some remarkable similarities between the chemical composition of EMP stars in dSphs and EMP stars in the halo of the Milky Way (Cohen & Huang 2009, 2010; Kirby et al. 2009; Frebel et al. 2010a,b; Simon et al. 2010; Tafelmeyer et al. 2010; Norris et al. 2010a,b; Lai et al. 2011; Gilmore et al. 2013; Frebel et al. 2014; Koch & Rich 2014; Roederer & Kirby 2014; Simon et al. 2015; Jablonka et al. 2015; Ji et al. 2016). These results hint, at some level, of universality in early chemical evolution and suggest that some of the most metal-poor stars in the Milky Way halo could have formed in dwarf galaxies. Because of the rarity of EMP stars, further identification and study of these objects in any dwarf galaxy provides key information to further investigate these initial findings.

Chemically characterizing members of the Sculptor dSph galaxy has provided insights on its chemical evolution and formation using high-resolution spectroscopy of red giant stars (Shetrone et al. 2003; Tolstoy et al. 2003; Geisler et al. 2005). Tolstoy et al. (2004) found evidence for two stellar components in Sculptor, as also seen in other dSphs. More recently, Kirby et al. (2009) and the DART team (Battaglia et al. 2008; Starkenburg et al. 2010; Romano & Starkenburg 2013) used samples of $\sim 400 - 600$ Sculptor stars to derive the metallicity distribution function (MDF). Later, Kirby et al. (2011) used the MDFs of Sculptor and other dSphs to investigate chemical evolution models. Additional modeling of Sculptor by de Boer et al. (2012) showed evidence for

* This paper includes data gathered with the 6.5 meter Magellan Telescopes located at Las Campanas Observatory, Chile.
[1] Department of Physics and Kavli Institute for Astrophysics and Space Research, Massachusetts Institute of Technology, Cambridge, MA 02139, USA; Email: achiti@mit.edu
[2] JINA Center for the Evolution of the Elements, USA
[3] Observatories of the Carnegie Institution for Science, 813 Santa Barbara St., Pasadena, CA 91101, USA
[4] Department of Astronomy, University of Michigan, Ann Arbor, MI 48109, USA
[5] Leiden Observatory, Leiden University, P.O. Box 9513, 2300RA Leiden, The Netherlands
[6] McWilliams Center for Cosmology, Department of Physics, Carnegie Mellon University, 5000 Forbes Avenue, Pittsburg, PA 15213, USA

extended star formation, and further modeling by Romano & Starkenburg (2013) suggested the importance of dilution and metal-removal in chemical evolution scenarios. Moreover, observations of a few individual EMP stars in Sculptor provided the first evidence that low-metallicity stars in dSphs are present and have chemical signatures matching those of EMP halo stars (Frebel et al. 2010a; Tafelmeyer et al. 2010). Further studies of the S abundances of stars in Scuptor have shown similarities with the halo at lower metallicities (Skúladóttir et al. 2015a), and studies of Zn abundances have suggested complex nucleosynthetic origins for the element (Skúladóttir et al. 2017). Recently, work by Simon et al. (2015) and Jablonka et al. (2015) has indicated that EMP stars in Sculptor may have been enriched by just a handful of supernovae from the first generation of stars.

The population of stars with [Fe/H] < -2.5 in the Milky Way halo has long been known to include a large fraction enhanced in carbon (Beers et al. 1992; Rossi et al. 1999; Aoki et al. 2002; Ryan 2003; Beers & Christlieb 2005; Cohen et al. 2005; Aoki et al. 2007a; Placco et al. 2014; Frebel & Norris 2015). This discovery led to the classification of carbon-enhanced metal-poor (CEMP) stars (metal-poor stars with [C/Fe] > 0.7), within which exist subdivisions contingent on the enhancements of r-process and/or s-process elements. Of those, CEMP-s and CEMP-rcd /s stars are readily explained as the products of binary mass transfer from an asymptotic giant branch (AGB) companion (Lucatello et al. 2005; Hansen et al. 2016). However, stars that show [C/Fe] enhancement reflecting the chemical composition of their formative gas cloud, as is thought to be the case for CEMP-r and CEMP-no stars, are the most useful in constraining theories of early chemical evolution. Proposed mechanisms behind this early carbon enhancement include "mixing and fallback" SNe and massive rotating stars with large [C/Fe] yields, as discussed in e.g., Norris et al. (2013).

Interestingly, the current sample of stars in Sculptor with [Fe/H] < -2.5 from Starkenburg et al. (2013), Simon et al. (2015), and Jablonka et al. (2015) contains no CEMP stars, contrary to expectations set by the high fraction of CEMP halo stars and earlier results that low-metallicity chemical evolution appears to be universal. Only one CEMP-no star has been previously detected in Sculptor (Skúladóttir et al. 2015b), with [Fe/H] = –2.03 and [C/Fe] ~ 0.51, and only three CEMP-s stars are known in the galaxy out of spectroscopic samples of hundreds of stars (Lardo et al. 2016; Salgado et al. 2016). Under the assumptions that the ancient analogs of today's dwarf galaxies formed the Milky Way halo, one would expect that dwarf galaxies should show carbon enhancement in their oldest stellar population as well. Earlier work detected a number of carbon-strong stars in dSph galaxies, including Sculptor, but did not report individual metallicities for stars, precluding the characterization of these detected carbon-strong stars as CEMP stars (Cannon et al. 1981; Mould et al. 1982; Frogel et al. 1982; Richer & Westerlund 1983; Aaronson et al. 1983; Blanco & McCarthy 1983; Azzopardi et al. 1985, 1986). More recent searches in dSph galaxies (Lai et al. 2011; Shetrone et al. 2013; Starkenburg et al. 2013; Skúladóttir et al. 2015b; Kirby et al. 2015; Susmitha et al. 2017) have, however, detected only a handful of any category of CEMP stars.

To investigate this apparent dearth of true CEMP stars, or CEMP-no stars, we surveyed Sculptor with the goal of identifying EMP star candidates and robustly characterizing its metal-poor population (Hansen et al., in prep). We conducted follow-up observations of the most promising of these candidates to establish the low-metallicity tail of the MDF of Sculptor, and constrain the CEMP fraction in the system. In this paper, we present [Fe/H] and [C/Fe] measurements of the stars in our sample. In Section 2, we provide an overview of the target selection and observations. In Sections 3 and 4, we outline our methods of obtaining [Fe/H] and [C/Fe] abundances for our sample. In Section 5, we discuss additional measurements and considerations that are useful in analyzing our sample. We present our results, discuss implications, and conclude in Section 6.

2. OBSERVATIONS AND DATA REDUCTION

2.1. *Target Selection*

We first obtained low-resolution ($R \approx 700$) spectroscopy of eight fields in Sculptor using the f/2 camera of the IMACS spectrograph (Dressler et al. 2011) at the Magellan-Baade telescope at Las Campanas Observatory. Each IMACS field spans a diameter of $27.4'$, and the eight fields together produce nearly complete coverage of the upper three magnitudes of Sculptor's red giant branch (RGB) over a $37' \times 39'$ area centered on the galaxy, which approximately corresponds to complete coverage out to ~ 2 times the core radius of Sculptor (Battaglia 2007). The IMACS observations were taken with a narrow-band Ca K filter attached to a 200-lines mm^{-1} grism. With this setup, approximately 900 stars can be observed at a time. IMACS targets were selected from the photometric catalog of Coleman, Da Costa, & Bland-Hawthorn (2005) using a broad window surrounding the RGB so as not to exclude stars at the extremes of the metallicity distribution. The selection limits were based on a Padova isochrone (Marigo et al. 2008) passing through the Sculptor RGB, and extended from 0.37 mag bluer than the isochrone to 0.19 mag redder than the isochrone in $V - I$, down to $V = 20$.

We selected Sculptor stars from the IMACS spectra for more extensive spectroscopic follow-up observations. We identified a sample of low-metallicity candidates by searching for stars with the smallest Ca K equivalent widths, adjusting for the color of each star according to the calibration of Beers et al. (1999). The most metal-poor known Sculptor stars from Frebel et al. (2010a) and Tafelmeyer et al. (2010) were independently recovered in this data set, as well as two new [Fe/H] < -3.5 stars (Simon et al. 2015). We then obtained $R \sim 4000$ and $R \sim 6000$ optical spectra of 22 of the best candidates, using the MagE spectrograph (Marshall et al. 2008) at the Magellan telescopes. The majority of the observed stars were confirmed as EMP stars, including a number with spectra dominated by carbon features.

2.2. *M2FS Observations*

Having confirmed the utility of the IMACS data for both identifying EMP and carbon-rich candidates in

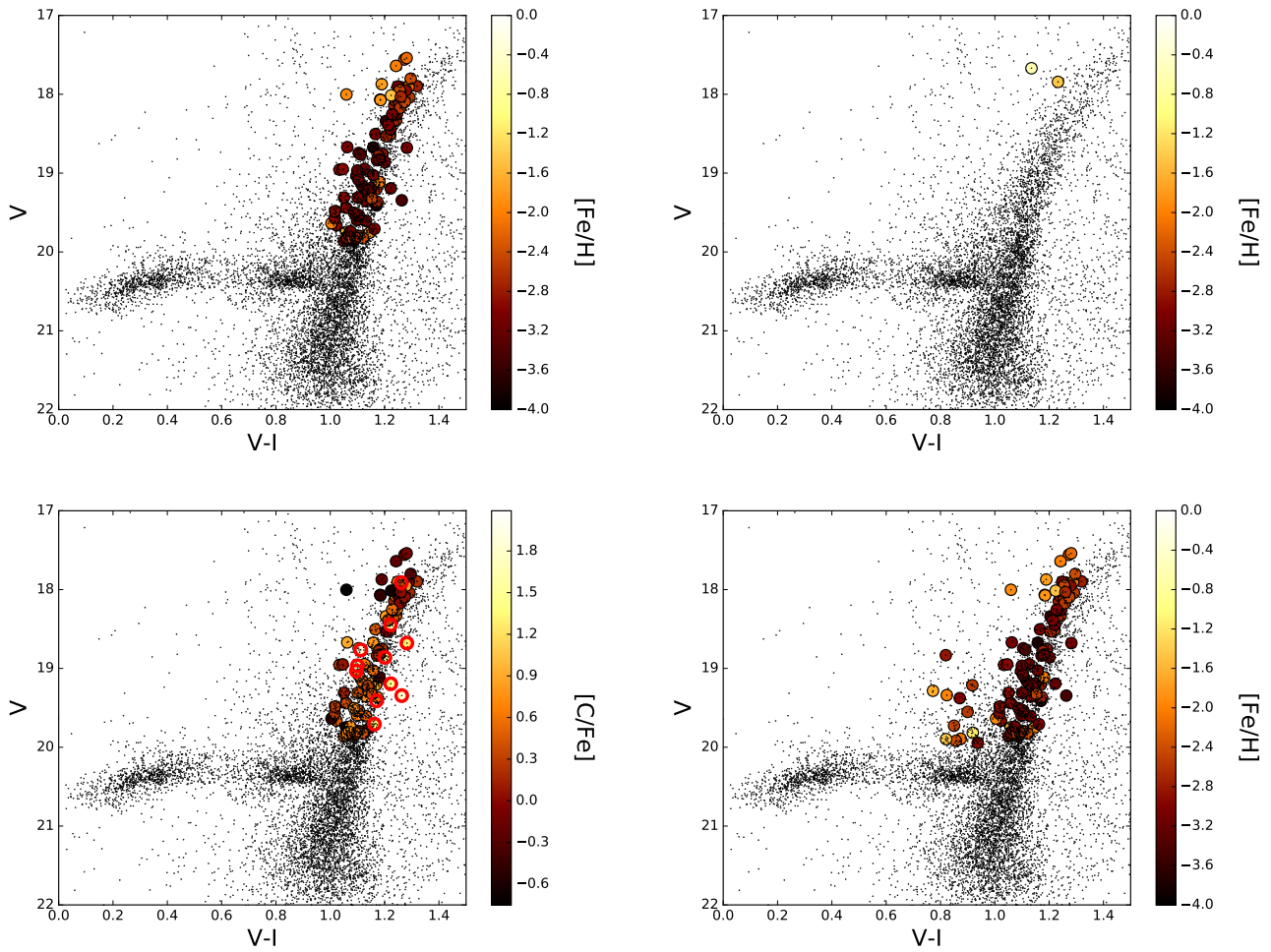

FIG. 1.— Color magnitude diagrams (CMDs) of Sculptor from Coleman et al. (2005). M2FS targets for which [Fe/H] and [C/Fe] are computed are over plotted. Top left: [Fe/H] of stars on the red giant branch of Sculptor that were selected as the most metal-poor candidates. Top right: [Fe/H] of bright stars that were selected to fill available fibers. Much of the bright star sample was excluded from this work (see Section 3.3). Bottom left: [C/Fe] of stars on the red giant branch of Sculptor that were selected to be metal-poor. Stars with saturated G-bands are circled in red. Bottom right: [Fe/H] of all stars we observed that were selected to be metal-poor.

Sculptor, we set out to obtain medium-resolution spectra of a much larger number of EMP candidates. We observed two partially overlapping 29.5′-diameter fields in Sculptor using the Michigan/Magellan Fiber System (M2FS) (Mateo et al. 2012) on the Magellan–Clay telescope. We employed the low-resolution mode of M2FS, producing $R = 2000$ spectra covering $3700 - 5700$ Å for 256 fibers.

M2FS targets were selected in two categories. First, we chose all of the EMP candidates from the IMACS sample (including those confirmed as low metallicity and/or carbon-rich with MagE spectra). Since these candidates only occupied about half of the M2FS fibers, we then added a magnitude-limited "bright" sample containing all stars along the Sculptor RGB brighter than $V = 18.1$ in field 1 and $V = 18.0$ in field 2 (the difference between the two reflects the number of fibers available and the number of bright stars in each field). This bright sample should be unbiased with respect to metallicity or carbon abundance. About 30 fibers per field were devoted to blank sky positions. A few broken fibers were not used. The first M2FS field, centered at RA (J2000), Dec (J2000) = 00:59:26, −33:45:19, was observed for 5×900 s on the night of 23 November, 2013. The second M2FS field, centered at 01:00:47, −33:48:39 was observed for a total of 6838 s on 14 September, 2014. Figure 1 shows the M2FS targets for which [Fe/H] and [C/Fe] were measured in this work on color magnitude diagrams of Sculptor. We note that stars with saturated CH G-bands are circled in red in the bottom left panel of Figure 1. While the most carbon-enhanced stars do appear to be biased redward of the Sculptor RGB, they are not excluded from our selection procedure.

M2FS data were reduced using standard reduction techniques (Oyarzún et al. 2016). We first bias-subtracted each of the four amplifiers and merged the data. We then extracted 2D spectra of all the fibers by using the spectroscopic flats to trace the location of science spectra on the CCD, flattened the science data, and took the inverse variance weighted average along the cross-dispersion axis of each science spectrum to extract a 1D spectrum.

We computed wavelength solutions using spectra of HgArNeXe and ThAr calibration arc lamps. The typical dispersion of our wavelength solution was ~ 0.10 Å, which we derived by fitting third-degree polynomials to

the calibration lamp spectra for the 2013 data. We derived the wavelength solution for the 2014 data by fitting third-degree Legendre polynomials. We performed the sky-subtraction by fitting a fourth-order b-spline to the spectra of ~ 10 sky fibers on the CCD, and fitting a third-order polynomial to the dependence of these spectra on the cross-dispersion direction of the CCD (e.g., the location of the fiber's output on the CCD). We then subtracted the predicted sky model at the location of each science spectrum on the CCD, and extracted final 1D spectra.

2.3. *Follow-up MagE Observations*

Motivated by the number of EMP and CEMP candidates from the M2FS data, we observed an additional ten Sculptor stars using the MagE spectrograph on the Magellan-Baade telescope in September 2016. This brought the total number of Sculptor stars observed with MagE to 31 stars, as one star had already been observed as part of the original 22 star sample (see Section 2.1). Five of these ten stars showed strong carbon features in their M2FS spectra. Another five were not seen to be as carbon-enhanced from their M2FS spectra, but we chose to observe them due to their similar stellar parameters to the strongly carbon-enhanced stars. These ten stars were analyzed to corroborate our M2FS carbon measurements. We also observed the halo CEMP-r/s star CS29497-034 for reference purposes. Five stars (four CEMP candidates and CS29497-034) were observed with the $0.7''$ slit ($R \sim 6000$), which granted sufficient resolution to resolve barium lines at 4554 Å, 4934 Å, 5853 Å, 6141 Å, and 6496 Å. The remaining stars were observed with the $1.0''$ slit ($R \sim 4000$). The MagE spectra were reduced using the Carnegie Python pipeline described by Kelson (2003). With these observations, we confirmed the CEMP and regular metal-poor nature of our candidates, as suggested by the M2FS observations.

3. METALLICITY MEASUREMENTS

We used established calibrations of two spectral line indices to measure [Fe/H] from the M2FS spectra. The first such index is the KP index, a measure of the equivalent width of the Ca II K line at 3933.7 Å. The second index is the LACF index, a line index derived from applying the autocorrelation function (ACF) to the wavelength range 4000 Å to 4285 Å, which is chosen due to the presence of many weak metal lines. Both line indices, along with the nature of their calibration to [Fe/H] values, are thoroughly discussed by Beers et al. (1999) and their implementation in this work is detailed in this subsection.

3.1. *Membership Selection*

We measured radial velocities for each star primarily to exclude non-members of Sculptor. Radial velocities were measured by cross-correlating the spectrum of each star with a rest-frame spectrum of the metal-poor giant HD122563. Wavelength calibration for spectra obtained in 2013 was carried out using a ThAr lamp, resulting in a well calibrated range from 3900 Å to 5500 Å. For the cross-correlation, we used this full range to determine velocities. However, spectra obtained in 2014 had associated HgArNeXe arc lamp frames taken, which provided fewer usable reference lines. It was found that cross-correlating over only the Hβ line (4830 Å to 4890 Å) gave the most precise ($\sim$10 km s^{-1}) velocity measurements for these spectra. Moreover, velocities obtained from the M2FS fiber observations in 2014 had to be adjusted to ensure that the mean velocity of the stars was centered on the velocity of Sculptor. Accordingly, velocities measured based on fiber observations on the red CCD chip were increased by 35 km s^{-1}. Those from the blue CCD chip observations were increased by 31 km s^{-1}. For stars on both the 2013 and 2014 fiber plates, we used the velocity measurement from the 2013 spectrum.

We assumed that stars with velocities within 35 km s^{-1} of the systemic velocity of Sculptor were members. This threshold corresponded to roughly 2.5σ of our distribution of velocities after excluding outliers. We found that applying this membership criterion recovered known members of Sculptor from Walker et al. (2009) and Kirby et al. (2009). Using this criterion, we excluded four stars in our sample that would otherwise have been part of this data set.

3.2. *Stellar Parameters*

We derive initial $B-V$ color, $T_{\rm eff}$, and $\log g$ estimates of stars in our IMACS sample by transforming V and I band photometry from Coleman et al. (2005) using a 12 Gyr, [Fe/H] $= -2.0$ Dartmouth isochrone (Dotter et al. 2008). After a first pass measurement of [Fe/H] with this initial $B-V$ estimate (see Section 3), we iteratively update the metallicity of the isochrone and re-derive parameters until convergence. Before any measurement of [Fe/H], the spectrum was shifted so that the Ca II K line was centered at 3933.7 Å. This re-centering was necessary given that the wavelength calibration was not necessarily accurate around the Ca II K feature, since only there was only one line below 4000 Å (a weak Ar II line at 3868.53 Å) in our arc frames.

3.3. *KP Index*

The KP index is a measurement of the pseudo-equivalent width of the Ca II K line at 3933.7 Å. To determine final KP indices, we first compute the K6, K12, and K18 indices using bandwidths of $\Delta\lambda = 6$ Å, 12 Å, and 18 Å, respectively, when calculating the equivalent width of the Ca II K feature (Beers et al. 1990). Table 1 lists the bands of these indices. The KP index assumes the value of the K6 index when K6 < 2 Å, the K12 index when K6 > 2 Å and K12 < 5 Å, and the K18 index when K12 > 5 Å.

To derive an estimate of the local continuum around the Ca II K feature, we fit a line through the red and blue sidebands listed in Table 1. We then visually inspected each continuum placement and applied a manual correction for a small subset of our sample that had an obviously bad fit (e.g., due to low S/N or nearby absorption features). After continuum normalization, we derived estimates of the K6, K12, and K18 indices using two methods. For the first approach, we directly integrated across the line band to estimate the pseudo-equivalent width. For the second approach, we integrated over the best-fit Voigt profile to the Ca II K line as illustrated in Figure 2. These two methods gave largely similar results, but the

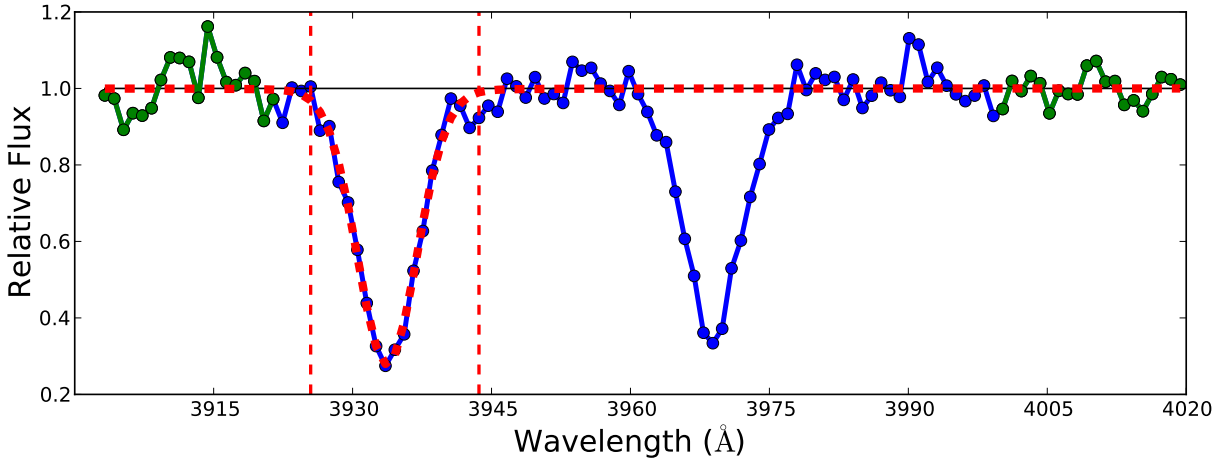

FIG. 2.— Spectral region around the Ca II K line (3933.7 Å) after continuum normalization. The horizontal black dashed line depicts the continuum fit to the blue and red sidebands (green), and the vertical red dashed lines correspond to the range of integration for the KP index. The over-plotted dashed red line corresponds to the best fit Voigt profile.

TABLE 1
KP LINE INDICES (Å)

Line Index	Blue Sideband	Red Sideband	Band
K6	3903−3923	4000−4020	3930.7−3936.7
K12	3903−3923	4000−4020	3927.7−3939.7
K18	3903−3923	4000−4020	3924.7−3942.7

KP values from direct integration were adopted to ensure consistency with previous work involving the calibration. We derive [Fe/H] values using the KP index and $B-V$ color as inputs to the Beers et al. (1999) calibration.

The KP index calibration from Beers et al. (1999) is only valid for stars with $B-V \leq 1.2$, meaning it can only be readily applied to 100 stars in our sample. This population largely excludes the bright-star sample, which is unbiased with respect to metallicity.

3.4. *LACF Index*

The LACF index measures the strength of many weak metal lines between 4000 Å and 4285 Å (Ratnatunga & Freeman 1989; Beers et al. 1999). It is computed by taking the autocorrelation of a spectrum within the aforementioned wavelength range after excising extraneous line features. The LACF index is then defined as the log of the value of the autocorrelation function (ACF) at $\tau = 0$ as defined in Equation 1 over this interval.

To ensure we computed the LACF index in a manner consistent with Beers et al. (1999), we closely reproduced their methodology. We first interpolated each spectrum using a cubic spline and re-binned in 0.5 Å increments to match their calibration sample. We then excised the ranges 4091.8 Å to 4111.8 Å and 4166 Å to 4216 Å to remove effects from the Hδ region and CN molecular absorption, respectively. To calculate the continuum, each of the three resulting ranges were independently fit by a fourth-order polynomial, after which outliers 2σ above and 0.3σ below each fit were excluded. An acceptable continuum estimate was returned after four iterations of this process.

After normalizing each wavelength segment by its corresponding continuum estimate, we re-stitched the three segments together and computed the power spectrum of the resulting spectrum. We then set the high and low frequency components of the power spectrum to zero in order to remove the effects of high frequency noise and continuum effects, respectively. The inverse Fourier transform of the power spectrum was taken to derive the ACF, which was then divided by the square of the mean counts in the normalized region. We finally computed the LACF index by taking the log of the resulting ACF at $\tau = 0$.

It is important to note that an alternative expression of the autocorrelation function is

$$\mathrm{ACF}(\tau) = \int_{\nu_1}^{\nu_2} f(\lambda+\tau)\bar{f}(\lambda)d\lambda \qquad (1)$$

where $\bar{f}(\lambda)$ is the complex conjugate of the function $f(\lambda)$. From Equation 1, it is clear that computing the LACF index, defined as the log of the value of the ACF at $\tau = 0$, is analogous to integrating the squared spectrum after manipulating Fourier components to remove continuum and noise related effects. This fact motivates the application of an ACF to measure line strength. As with the KP index, the LACF index is only calibrated to [Fe/H] for stars with $B-V \leq 1.2$ (see discussion in Section 3.3).

3.5. *Comparison of Methods and Final [Fe/H] Values*

To ensure our measured KP and LACF indices were consistent with the existing [Fe/H] calibration, we measured KP and LACF indices on a subset of the calibration sample in Beers et al. (1999). We found agreement in KP indices, but a gradually increasing scatter in LACF measurements when LACF < 0, which roughly corresponds to very metal-poor stars, stars with high effective temperatures, or stars with spectra that have low signal-to-noise. We thus chose to discard the LACF-based metallicity measurement for stars with LACF < -0.5 or when $[\mathrm{Fe/H}]_{\mathrm{KP}} < -2.5$. Since the LACF works best at measuring [Fe/H] in the more metal-rich regime where weak metal lines are more prominent, this exclusion seems reasonable. We also chose to discard KP-based metallicity measurements when $[\mathrm{Fe/H}]_{\mathrm{KP}} > -1.0$, motivated by the failure of the KP calibration at high metallicities due to the saturation of the Ca II K line. In the regime where

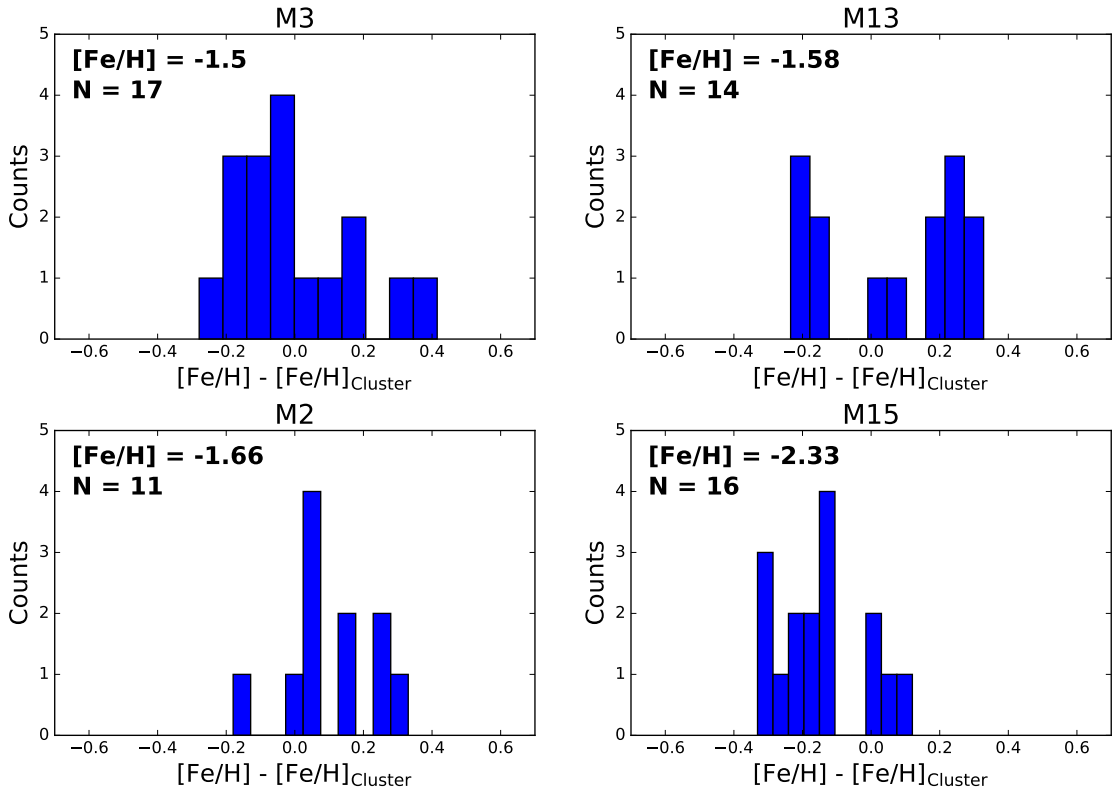

FIG. 3.— Histograms of the difference between our measured metallicity of each globular cluster member and the overall cluster metallicity for globular clusters M3 (top left), M13 (top right), M2 (bottom left), and M15 (bottom right).

both KP and LACF based metallicities are valid, we take the average of the two measurements weighted by the measurement uncertainty.

The α-element abundance of stars in the Beers et al. (1999) calibration is assumed to be $[\alpha/\mathrm{Fe}] = +0.4$ for $[\mathrm{Fe/H}] < -1.5$ and $[\alpha/\mathrm{Fe}] = -0.27\times[\mathrm{Fe/H}]$ for $-1.5 < [\mathrm{Fe/H}] < 0$. Stars in Sculptor display a different trend in $[\alpha/\mathrm{Fe}]$ with [Fe/H]. We account for this discrepancy by first computing an $[\alpha/\mathrm{H}]$ measurement for our stars based on the aforementioned α-element trends used in the Beers calibration for both the KP and LACF derived metallicities. We then fit a line to a Sculptor [Fe/H] vs. $[\alpha/\mathrm{H}]$ trend derived from measurements in Kirby et al. (2009), and use this trend to compute an [Fe/H] measurement from our $[\alpha/\mathrm{H}]$ measurement for each of our Sculptor stars. This adjustment is motivated by the fact that the Beers et al. (1999) calibrations measure the strength of α-element features and derive metallicities under the assumption of a given $[\alpha/\mathrm{Fe}]$ for halo stars, which is discrepant from the trend in dwarf galaxy stars. This correction typically increased the metallicities of stars in our sample by $\lesssim 0.1$ dex, since it had no effect on stars with $[\mathrm{Fe/H}] < -3.0$ and increased metallicities of stars with $[\mathrm{Fe/H}] = -2.5$ by ~ 0.1 dex.

Initial [Fe/H] uncertainties were assigned following Beers et al. (1999). To account for uncertainties in using an isochrone to transform between $V-I$ and $B-V$ color, we propagated the uncertainty in our original $V-I$ color to the final [Fe/H] measurements and added this effect in quadrature to the other uncertainties. We also propagated uncertainties in the age of the isochrone, which had negligible effects. Finally, we re-measured the metallicities after shifting the continuum by the standard errors of the fluxes in the red and blue continuum regions. The difference between the re-measured metallicities and the original metallities was added in quadrature with the other estimates of uncertainty. Typical uncertainties are $\sim$0.25 dex.

3.6. *External Validation: Comparison to Globular Cluster Members*

As an external check on our metallicity measurements, we determined [Fe/H] values for cool ($T_{\rm eff} < 5500$ K) member stars in four globular clusters (M2, M3, M13, M15) with metallicities ranging from $[\mathrm{Fe/H}] = -2.33$ to -1.5. We retrieved medium-resolution spectra of these stars from the Sloan Digital Sky Survey-III[1] (Eisenstein et al. 2011; Ahn et al. 2014). $V-I$ colors were derived by applying an empirical color transformation following Jordi et al. (2006).

The metallicity spread among members of a globular cluster is a fraction of our measurement uncertainties, with the exception of some anomalies in M2 (Yong et al. 2014). Thus, we used the offset of our [Fe/H] values of each cluster member from the average metallicity of the globular cluster to gauge the validity of our metallicity calibration. Before measuring metallicities, we recorded the mean $[\alpha/\mathrm{Fe}]$ of these globular clusters from Carney

[1] http://dr10.sdss3.org

TABLE 2
Stellar Parameter Comparison

ID	$\log g_{\rm MR}$	$\log g_{\rm HR}$	$T_{\rm eff_{MR}}$ (K)	$T_{\rm eff_{HR}}$ (K)	$[{\rm Fe/H}]_{\rm KP}$	$[{\rm Fe/H}]_{\rm HR}$	Δ[Fe/H]	Ref.
S1020549	1.30	1.25	4610	4702	-3.74 ± 0.21	-3.68	-0.06	S15
Scl 6_6_402	1.67	2.00	4796	4945	-3.91 ± 0.25	-3.53	-0.38	S15
Scl 11_1_4296	1.52	1.45	4716	4770	-3.90 ± 0.21	-3.77	-0.13	S15
Scl 07−50	1.35	1.05	4676	4558	-3.96 ± 0.20	-4.05	$+0.09$	S15
S1020549	1.29	1.25	4581	4702	-3.63 ± 0.21	-3.68	$+0.05$	S15
Scl 11_1_4296	1.55	1.45	4697	4770	-3.33 ± 0.22	-3.77	$+0.44$	S15
Scl 07−50	1.40	1.05	4641	4558	-3.77 ± 0.20	-4.05	$+0.28$	S15
ET0381	1.19	1.17	4532	4540	-2.83 ± 0.19	-2.83	$+0.00$	J15
Scl_03_059	1.10	1.10	4492	4400	-3.00 ± 0.15	-3.20	$+0.20$	J15

Note. — $[{\rm Fe/H}]_{\rm KP}$ is the metallicity measured by applying the KP index calibration. $[{\rm Fe/H}]_{\rm HR}$ is the metallicity measured in the indicated reference paper. Measurements labeled MR are medium-resolution measurements following the methodology of this paper. Top section: Measurements from smoothed high-resolution spectra of stars presented in Simon et al. (2015). Bottom section: Measurements from our medium-resolution M2FS spectra. S15 and J15 refer to Simon et al. (2015) and Jablonka et al. (2015), respectively. Log g values in this table have been corrected by +0.39 dex to account for the measured offset with respect to Kirby et al. (2010).

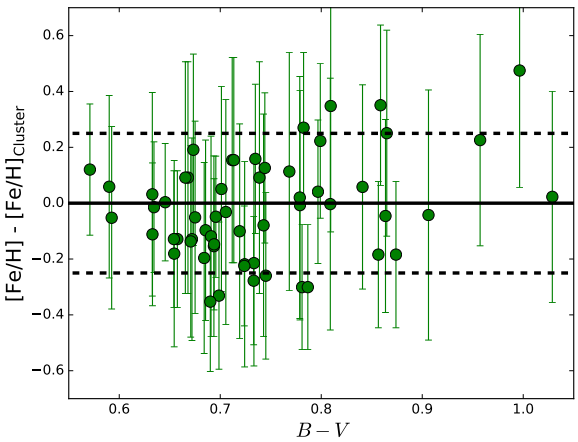

Fig. 4.— Difference between our measured metallicity of each cluster member and the overall cluster metallicity as a function of $B-V$ color. Dashed lines correspond to ± 0.25 dex. The mean of the distribution of residuals is -0.02 and the standard deviation is 0.18.

(1996), Kirby et al. (2008), and Yong et al. (2014) and corrected them for the discrepant [α/Fe] assumption in our calibrations. As shown in Figures 3 and 4, our measurements gave largely reasonable results, with an overall [Fe/H] offset of -0.02 dex and scatter of 0.18 dex. This is consistent with our typical derived uncertainty in [Fe/H] of $\sim$0.25 dex.

3.7. *External Validation: Comparison to Kirby et al.*

Kirby et al. (2009, 2010, 2013) measured the metallicities and α-abundances of a total of 391 stars in Sculptor with medium-resolution spectroscopic data from the Deep Imaging Multi-Object Spectrometer on the Keck II telescope. We found 86 stars in common with our full sample of $\sim$ 250 stars, of which 20 stars have $B-V \leq 1.2$. We compare the stellar parameter measurements between all 86 stars. We find reasonable agreement in our $T_{\rm eff}$ measurements as demonstrated by a mean offset of $\overline{\Delta T_{\rm eff}} = 25$ K and a standard deviation of $\sigma(\Delta{\rm Teff}) = 137$K. For $\log g$, we correct the significant offset of +0.39 dex compared to the Kirby et al. sample. The mean difference in $\log g$ after this correction is 0, with a standard deviation of 0.17 dex. If we were to only consider stars with $B-V \leq 1.2$, then the standard deviation would be 0.23 dex. This correction also results in agreements with $\log g$ values of stars with high-resolution spectroscopic stellar parameters (see Table 2). We note that not applying this gravity correction would artificially increase the carbon abundance correction we apply to take into account the evolutionary state of the star (see Placco et al. 2014), and thus the number of CEMP stars in the sample. We then compare our metallicities for the subset of stars with $B-V \leq 1.2$. We find a mean offset of $[{\rm Fe/H}] - [{\rm Fe/H}]_{\rm K10} \approx -0.11$ dex with a standard deviation of ~ 0.15 dex (excluding two outliers below $B-V = 1.2$ for which we measure a lower metallicity by over ~ 0.5 dex, see Figure 5). Including these outliers changes the mean offset to $[{\rm Fe/H}] - [{\rm Fe/H}]_{\rm K10} \approx -0.16$ dex and increases the scatter to ~ 0.19 dex.

Both outliers (10_8_2730 and 10_8_2788) in Figure 5 have low reported calcium abundances ([Ca/Fe]=$-0.23\pm$ 0.30 and [Ca/Fe] = 0.05$\pm$0.39) in Kirby et al. (2010). This could lead to a weaker Ca II K line than our assumed [α/Fe] would suggest and would cause an underestimation of the metallicity.

Figure 5 also demonstrates the failure of the KP and ACF calibrations for $B-V > 1.2$. Accordingly, we choose to limit this work to the subset of stars in our sample with $B-V \leq 1.2$.

3.8. *External Validation: Comparison to High-Resolution [Fe/H]*

As a final check to ensure the KP calibration holds for extremely metal-poor (EMP) stars, we retrieved high-resolution spectra of four EMP Sculptor members from Simon et al. (2015)[2]. We smoothed these spectra to match the resolution of our medium-resolution data and degraded the signal-to-noise ratio to 20 Å^{-1}. We then computed KP-derived metallicities of these stars. The results are shown in the top portion of Table 2 and demonstrate the accuracy of KP calibration.

We also compared the KP-derived metallicities from our M2FS sample to high-resolution measurements in Simon et al. (2015) and Jablonka et al. (2015) for five stars in common to both samples. The results are shown in the bottom panel of Table 2. We note a marginally

[2] The spectrum of the fifth star in that paper does not extend blue-ward to the Ca II K feature.

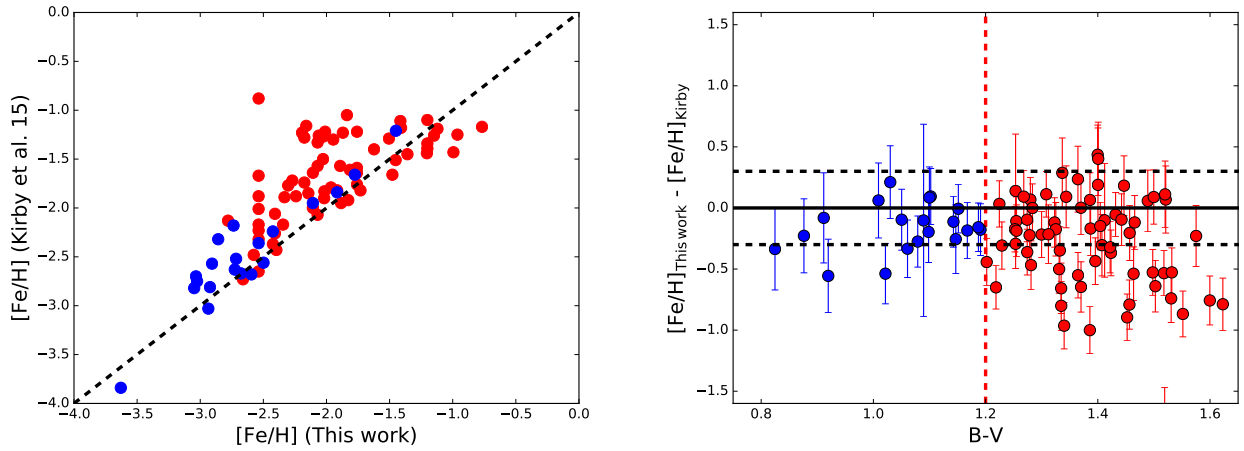

FIG. 5.— Left: Comparison of [Fe/H] measured by Kirby et al. (2010) and [Fe/H] measured in this work for the 86 stars in both samples. Blue points correspond to stars with $B-V \leq 1.2$ and red points correspond to stars with $B-V > 1.2$. Right: The difference between [Fe/H] measured in this work and [Fe/H] measured by Kirby et al. (2015) as a function of $B-V$ color. The vertical line marks the cutoff to the right of which $B-V$ colors are not directly calibrated to [Fe/H] in Beers et al. (1999). Dashed lines indicate ±0.30 dex.

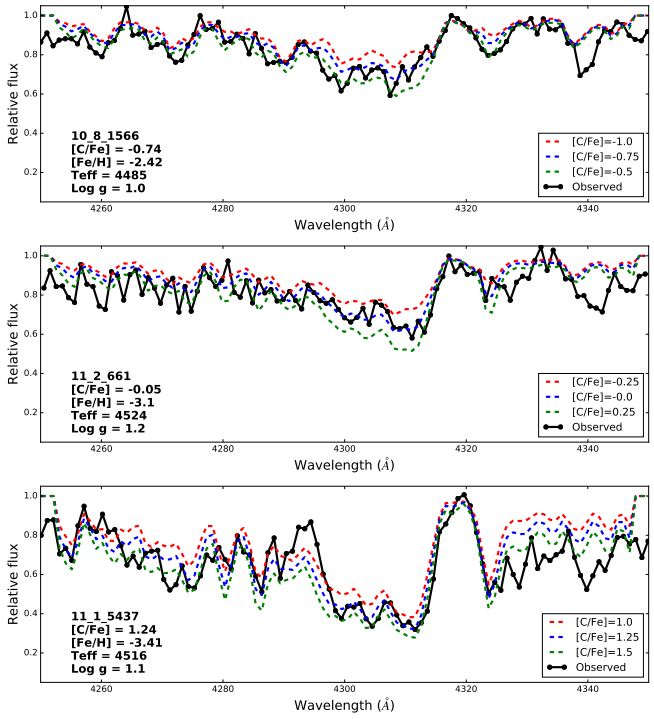

FIG. 6.— Spectral region around the G-band together with best fitting synthetic spectra (blue) for three example observed M2FS spectra (black). Synthetic spectra with [C/Fe] closest to the 1σ upper and lower [C/Fe] measurements are overplotted in red and green, respectively.

higher KP-derived metallicity in most cases for the EMP stars in the M2FS data. The largest residual (11_1_4296) can reasonably be explained due to the presence of noise near the Ca II K line. Interpolating over this noise spike results in a marginally lower disagreement of +0.34 dex when compared to the high-resolution [Fe/H] measurement.

4. CARBON ABUNDANCE MEASUREMENTS

To derive carbon abundances ([C/Fe]), we matched each observed spectrum to a grid of synthetic spectra closely following the methodology of Kirby et al. (2015). We generated these using the MOOG spectrum synthesis code with an updated treatment of scattering (Sneden 1973; Sobeck et al. 2011), and model atmospheres from ATLAS9 (Castelli & Kurucz 2004). We independently computed [C/Fe] using regression relations from Rossi et al. (2005), but found that fitting to a grid allowed accurate [C/Fe] measurements over a broader range of input parameters.

4.1. *Spectrum Synthesis*

Table 3 lists the stellar parameters of the generated grid of synthetic spectra. We used a comprehensive line list spanning 4100 Å to 4500 Å compiled by Kirby et al. (2015). The list comprises transitions from the Vienna Atomic Line Database (VALD; Piskunov et al. 1995; Kupka et al. 1999), the National Institutes of Standards and Technology (NIST; Kramida et al. 2014), Kurucz (1992), and Jorgensen et al. (1996). We assumed an isotope ratio of $^{12}C/^{13}C = 6$ based on the low surface gravity ($\log g \leq 2.0$) of most of our stars. The α-element abundance of the grid was chosen to be +0.2 dex, which is the mean expected value for this sample of Sculptor members, as gleaned from measurements by Kirby et al. (2009). Each synthetic spectrum was degraded to match the resolution of medium-resolution M2FS spectra. This grid was then used for measuring the carbon abundances reported in this paper. It should have similar inputs (e.g., line lists, model atmospheres) to previous works on the CEMP fraction in dwarf galaxies (e.g., Kirby et al. 2015) and other studies of halo stars. This enables a fair comparison of our results with literature values.

To appropriately compare our [C/Fe] measurements with nearly all values in the literature, we generated two smaller test grids based on model atmospheres and line lists different from those in the primary grid used in our analysis. The first test grid was generated using the Turbospectrum synthesis code (Alvarez & Plez 1998; Plez 2012), MARCS model atmospheres (Gustafsson et al. 2008), and a line list comprised of atomic data from VALD, CH data from Masseron et al. (2014), and CN data from Brooke et al. (2014) and Sneden et al.

TABLE 3
Synthetic spectrum grid stellar parameter range

Parameter	Minimum	Maximum	Step
λ	4250 Å	4350 Å	0.01 Å
$T_{\rm eff}$	3700 K	5700 K	50 K
log g	0.0	4.0	0.5
[Fe/H]	−4.0	+0.2	0.2
[C/Fe]	−2.00	2.00	0.25

(2014). The second test grid had the same inputs as the first test grid, but was generated using MOOG to compare differences between just the two synthesis codes. Both test grids spanned 4500 to 4800 K in effective temperature, 1.0 to 2.0 dex in log g, and −4.0 to −2.5 dex in [Fe/H], which roughly covers the stellar parameters of the more metal-poor stars in our sample.

4.2. *Fitting to the Grid*

Since synthetic spectra computed by MOOG are generated as normalized spectra, we normalized each spectrum. We found that iteratively fitting a cubic spline to the observed data from 4100 Å to 4500 Å, excluding points 5σ above and 0.1σ below in each iteration, reproduced the continuum well. After dividing the observed spectrum by our continuum estimate, we found the best fitting synthetic spectrum by varying [C/Fe].

We then implemented a χ^2 minimizer to match the region spanning the CH G-band (4260 Å to 4325 Å) to the synthetic grid. We measured [C/Fe] by setting the three parameters $T_{\rm eff}$, log g, and [Fe/H] equal to the values determined from our medium-resolution M2FS measurements and letting [C/Fe] vary as a free parameter. We then interpolated between the five [C/Fe] measurements around the best [C/Fe] value with the lowest χ^2 values to determine a final carbon abundance. Sample fits are shown in Figure 6. Each [C/Fe] measurement was corrected to account for the depletion of carbon for stars on the upper red giant branch (Placco et al. 2014). After this correction, we find no statistically significant trend in the [C/Fe] abundances with respect to measured Log g values.

To determine the uncertainty in our carbon abundance measurements, we re-measured [C/Fe] 100 times for each spectrum after varying the stellar parameters each time. For each measurement of [C/Fe], we drew values of $T_{\rm eff}$, log g, [Fe/H] from gaussian distributions parametrized by the medium-resolution measurements and uncertainties of those parameters. We adopted stellar parameter uncertainties of ±150 K for $T_{\rm eff}$ and ±0.15 dex for log g. Before each measurement, the continuum was multiplied by a number drawn from a gaussian distribution centered on one with $\sigma = 0.01$ to capture the uncertainty in continuum placement. The standard deviation of the resulting [C/Fe] measurements was taken as the total uncertainty in our measurement.

4.2.1. *External Validation: Comparison to SkyMapper Sample from Jacobson et al. (2015)*

We applied our framework to measure [C/Fe] values to a sample of high-resolution Magellan/MIKE spectra of metal-poor halo stars selected from the SkyMapper survey. These spectra were degraded to match the resolution of our medium-resolution spectra and were injected with gaussian noise to bring the S/N down to 20 Å^{-1}. High-resolution [C/Fe] abundances computed by Jacobson et al. (2015) were used as reference values.

Analyzing a sample of 84 stars, we find that our [C/Fe] values differ from the high-resolution values [C/Fe] by a median value of 0.03 dex with $\sigma(\Delta[{\rm C/Fe}]) = 0.22$ dex (see Figure 7). We regard this agreement as excellent, since different normalization routines tend to produce different [C/Fe] measurements, given the difficulty of normalizing the G-band due to ubiquitous absorption features. Furthermore, the average offset is dwarfed by the typical measurement uncertainty of ∼ 0.35 dex. Raising the continuum placement by 2% increases [C/Fe] by ∼ 0.1 dex in this sample.

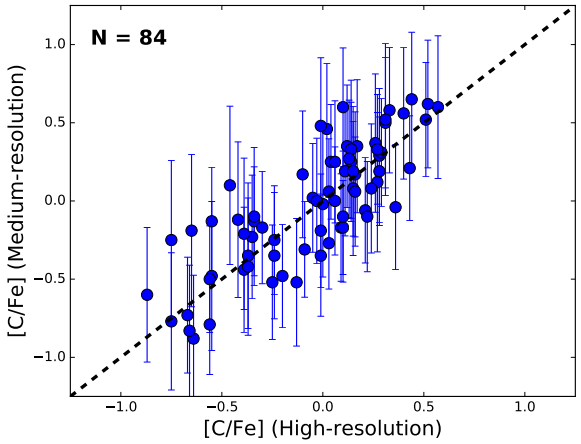

Fig. 7.— Carbon abundance measurements of metal-poor stars from Jacobson et al. (2015) after spectra were degraded to the same resolution as the Sculptor M2FS spectra versus high-resolution [C/Fe] measurements of the same stars. The median offset between medium-resolution and high-resolution [C/Fe] measurements is 0.03 dex and the observed scatter is 0.22 dex.

TABLE 4
[C/Fe] comparison with literature

ID	$[{\rm C/Fe}]_{\rm This\ work}$ (dex)	$[{\rm C/Fe}]_{\rm ref}$ (dex)	Δ[C/Fe] (dex)	Ref.
S1020549	< 0.25	< 0.20	–	S15
Scl11_1_4296	0.25 ± 0.32	0.34 ± 0.34	−0.09	S15
Scl07-50	< 0.34	-0.28 ± 0.34	–	S15
1008832	-1.14 ± 0.27	-0.88 ± 0.10	−0.26	K15
1007034	-1.01 ± 0.37	-1.11 ± 0.10	+0.10	K15
1007391	$+0.55 \pm 0.38$	-0.05 ± 0.13	+0.60	K15
1009538	-0.78 ± 0.61	-0.80 ± 0.11	+0.02	K15
1010633	-0.84 ± 0.31	-0.84 ± 0.10	0.00	K15
1013035	< 0.00	< -1.24	–	K15
1013808	< 0.22	-1.05 ± 0.27	–	K15
1016486	-0.26 ± 0.36	-0.65 ± 0.12	+0.39	K15
ET0381	-0.18 ± 0.34	-1.00 ± 0.15†	+0.82‡	J15
scl_03_059	-0.39 ± 0.40	-1.20 ± 0.40†	+0.81‡	J15

Note. — S15, K15, and J15 refer to Simon et al. (2015), Kirby et al. (2015), and Jablonka et al. (2015), respectively.
† Jablonka et al. (2015) present asymmetric uncertainties. These are the average of their asymmetric uncertainties.
‡ See Section 4.4 for a discussion of the potential causes of these discrepancies.

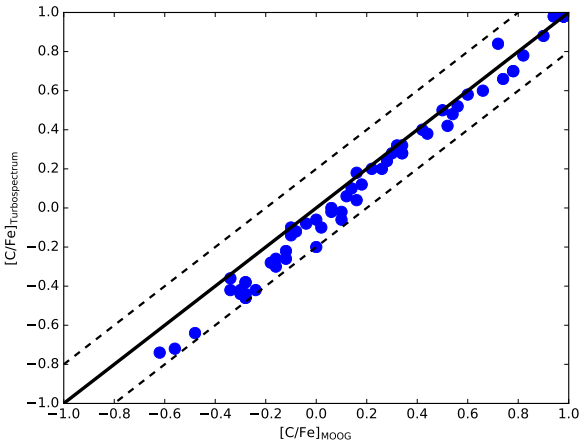

FIG. 8.— [C/Fe] measured with Turbospectrum, the MARCS model atmospheres, and the Masseron et al. (2014) line list vs. [C/Fe] measured with MOOG and the same inputs. Dashed lines indicate ±0.2 dex offsets to guide the eye.

4.3. *External Validation: Comparison to Kirby et al. (2015) and Simon et al. (2015)*

Three stars in our sample have high-resolution [C/Fe] measurements in Simon et al. (2015) with which we find agreement, as shown in Table 4. Eight stars in our sample have medium-resolution [C/Fe] measurements in Kirby et al. (2015). We find good agreement with their measurements, except for one star for which we measure a higher [C/Fe] by 0.6 dex. If we adopt the stellar parameters provided by Kirby et al. (2015), then the discrepancy reduces to 0.33 dex. This resulting discrepancy appears to be reasonable given the reported uncertainty in our [C/Fe] measurements of $\sim$ 0.35 dex and the low S/N of the M2FS spectrum of the star.

4.4. *External Validation: Comparison to Jablonka et al. (2015)*

Two stars in our sample have high-resolution [C/Fe] measurements in Jablonka et al. (2015). We do not find agreement in [C/Fe] measurements, as our measurements are at least $\sim$ 0.8 dex higher (see Table 4). We note that Jablonka et al. (2015) adopted $\log \epsilon(\mathrm{C})_\odot = 8.55$ (Anders & Grevesse 1989; Grevesse & Sauval 1998), which is discrepant with the $\log \epsilon(\mathrm{C})_\odot = 8.43$ assumed in MOOG (Asplund et al. 2009). This can account for 0.12 dex of the total [C/Fe] offset between the measurements.

To explore whether the rest of this discrepancy could reasonably be explained by differences in the spectrum synthesis codes, model atmospheres, or line lists, we first attempted to reproduce the synthesis shown in Jablonka et al. (2015) for star ET0381. We were able to reproduce their synthesis using Turbospectrum, the MARCS model atmosphere, and the Masseron line list, but noticed a consistent offset of $\sim$0.5 dex if we attempted to reproduce the synthesis with our adopted line list and MOOG. This total observed discrepancy between our two approaches reasonably accounts for most of the observed offset between [C/Fe] measurements, and about half of this observed $\sim$ 0.5 dex discrepancy can be ascribed to differences in the line lists and adopted solar abundances.

To ensure that our CEMP detections were not susceptible to differences in synthesis codes, line lists, and model atmospheres, we replicated our analysis for our CEMP stars using the two test grids discussed in Section 4.1. We measured [C/Fe] for the subset of stars falling within the grid. As shown in Figure 8, the discrepancies in [C/Fe] between the two synthesis codes are largely within 0.2 dex, but grow larger for carbon-poor stars. Different model atmospheres and input line lists cause up to another $\sim$ 0.1 to 0.2 dex difference. Referring to Figure 8, we note that a star such as ET0381 with a measurement of [C/Fe]~ -0.20 in MOOG tends to have an abundance lower by $\sim$ 0.15 dex in Turbospectrum. If we apply additional offsets accounting for differences in line lists and adopted solar abundances, we recover the aforementioned offset of $\sim$ 0.50 dex. However, the classification of carbon-enhanced stars appears to be largely robust to different synthesis codes, model atmospheres, and input line lists.

4.5. *Confirmation of [C/Fe] with MagE spectra and further classification*

Motivated by the high number of CEMP stars in the M2FS sample, we conducted follow-up observations of ten Sculptor stars with the MagE spectrograph as outlined in Section 2.3. This sample included five strong CEMP candidates, and five stars that were not as carbon-enhanced but had similar stellar parameters to the five CEMP candidates. We also observed one halo CEMP-r/s star, CS29497-034, as a comparison.

The purpose of these observations was to apply an independent check on our overall classification scheme, and to potentially derive the barium abundance of the stars to further classify them. Large Ba abundances in carbon-rich metal-poor stars are a strong indicator of the stars belonging to the CEMP-s and CEMP-r/s classes that are generally explained as being caused by accretion from a binary companion (Hansen et al. 2016). The more metal-rich analogs are the CH-strong and Ba-strong stars (McClure & Woodsworth 1990). Any of these stars have to be excluded when computing a CEMP fraction, as their carbon enhancement does not reflect the abundance pattern in their birth environment. We indeed verified the carbon-rich nature of the five stars in our sample, but found four of them to be more metal-rich stars of potentially either the CH-strong or Ba-strong class (see Section 5.1). The other star was observed with the 1″ slit, which does not provide sufficient resolution to measure barium features. M2FS spectra of a few strong carbon-enhanced stars are shown in Figure 9.

4.6. *Identifying accreting binary carbon-rich stars in our M2FS sample*

It is necessary to exclude carbon-rich stars whose source of enhancement is extrinsic (e.g. accretion from a binary companion) from our calculation of the CEMP fraction. Generally, members of this class of carbon-rich binary stars can be identified by radial velocity monitoring or by detecting a combined enhancement in s-process elements (e.g. Ba) together with carbon that would have been produced in a companion asymptotic giant branch star. But recent work by Yoon et al. (2016) suggests that stars with sufficiently high absolute carbon abundance (A(C)) can already be identified as CEMP-s stars just based on the [Fe/H] and A(C) measurements, as shown in Figure 10.

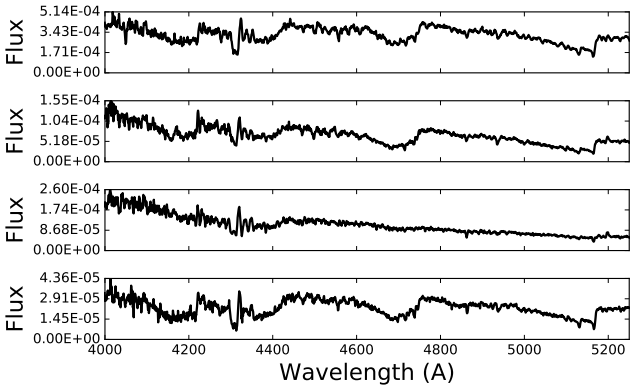

FIG. 9.— M2FS spectra of 4 stars (from top: 10_7_486, 10_8_3963, 11_1_4121, and 11_1_6440) that have saturated G-bands ($\sim$ 4315 Å). We measure their carbon abundance using the C2 band head at 5165 Å in their corresponding MagE spectra.

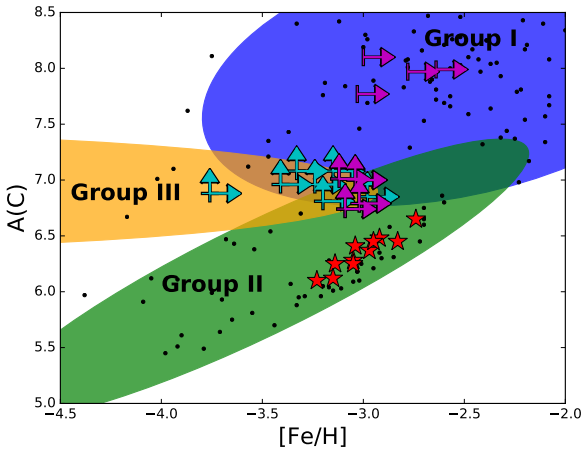

FIG. 10.— Yoon et al. plot with the original sample of halo stars in black and our Sculptor CEMP candidates overlaid in red, cyan, and magenta points. Groups I, II, and III are represented by blue, green, and orange ellipses, respectively. Cyan points correspond to M2FS measurements of stars with saturated G-bands and lower limits on their carbon abundances and metallicities, magenta points correspond to M2FS measurements of stars with saturated G-bands but accompanying MagE carbon abundance measurements, and magenta points in Group I are MagE measurements of those stars with saturated G-bands. The majority of Group I stars are CEMP-s stars, and the majority of Group II and III stars are CEMP-no stars

We can readily apply the Yoon et al. criterion to both our M2FS and MagE samples. However, for the four most carbon-enhanced stars in our MagE sample there is a discrepancy in our carbon abundance measurements. The A(C) values derived from the MagE data suggests these stars to be clearly s-process rich stars, while the M2FS A(C) measurements place them on the boundary according to the Yoon et al. criterion.

The higher resolution of the MagE spectra better resolves the G-band and the C_2 band head and suggests that these four stars are more carbon-enhanced than inferred from the lower resolution M2FS spectra. In addition, renewed inspection of the Ca II K line reveals the same trend; these four stars are actually more metal-rich than the KP index measurement from the M2FS data had indicated. Overall, these revisions strongly suggest that the four stars could be either CEMP-s stars (if they indeed have [Fe/H] $\lesssim -1.5$), or belong to the class of even more metal-rich CH-strong or Ba-strong stars.

Regarding the carbon abundance discrepancy, we note that when high carbon abundances lead to strong spectral absorption features (especially in cool stars), there is no region in the vicinity of the G-band (4250 Å to 4350 Å) to place the true continuum value in M2FS spectra. Thus, even accounting for this effect can still easily lead to systematically underestimating the continuum, and thus the carbon abundance. These four stars all had $[C/Fe]_{M2FS} \gtrsim 1$. We thus speculate that the G-band in M2FS spectra begins to saturate around $[C/Fe]_{M2FS} \sim 1$.

We note that the G-band in the higher-resolution MagE spectra also begins to saturate for those four stars. This is illustrated by our inability to use the G-band to recover the literature [C/Fe] measurement of CS29497-034, a star with similar G-band depth in the MagE spectra as our Sculptor members with high [C/Fe]. Motivated by the near-saturation of the G-band for these stars, we instead determined the carbon abundances of CS29497-034 using the C_2 band head at 5165 Å. We used a line list compiled from Sneden et al. (2009, 2016) and Masseron et al. (2014) and the MOOG synthesis code. We measure [C/Fe] = 2.6±0.1 for CS29497-034, consistent with the literature value of [C/Fe] = 2.72 (Aoki et al. 2007b). We thus use the C_2 band head to measure carbon abundances for the stars observed with MagE that have a near saturated G-band.

We find 11 stars with $[C/Fe]_{M2FS} > 1.0$ and showing the presence of a C_2 band head and a very strong G-band, which we suspect to have underestimated carbon abundances. If the A(C) value of these stars were revised upwards by $\sim$1 dex (following the results for CS29497-034 and the four stars also observed with MagE), they would clearly be members of the class of s-process rich stars, based on the Yoon et al. plot (see Figure 10). We thus consider these stars as s-process rich candidates, and list our derived carbon abundances strictly as lower limits in Table 6 and Figure 12. Table 5 has a final list of the iron and carbon abundances computed for the subset of all 31 MagE spectra with $B-V < 1.2$. Given the ambiguity in the metallicities of the carbon-rich stars observed with MagE, we cautiously only list A(C) measurements for those stars.

5. CHEMICAL SIGNATURES OF THE METAL-POOR STELLAR POPULATION OF SCULPTOR

5.1. *[Ba/Fe] estimates from MagE spectra & exclusion from CEMP-no classification*

In our follow-up MagE observations (Section 2.3) of ten stars, we observed four of the five very carbon-enhanced candidates with the 0.″7 slit to obtain sufficient resolution ($R \sim 6000$) to also resolve barium lines at 4554 Å, 4934 Å, 5853 Å, and 6141 Å. We used a line list from Sneden et al. (2009, 2016) and the MOOG synthesis code to synthesize these lines and constrain [Ba/Fe].

At $R \sim 6000$, these four lines can be blended, e.g., with praseodymium at 5853 Å, when neutron-capture element abundances are high as in s-process-rich stars. We are able to reproduce the literature [Ba/Fe] = 2.2 measurement of CS29497-034 when considering the depth of the centroid of the line and neglecting fitting the entire line

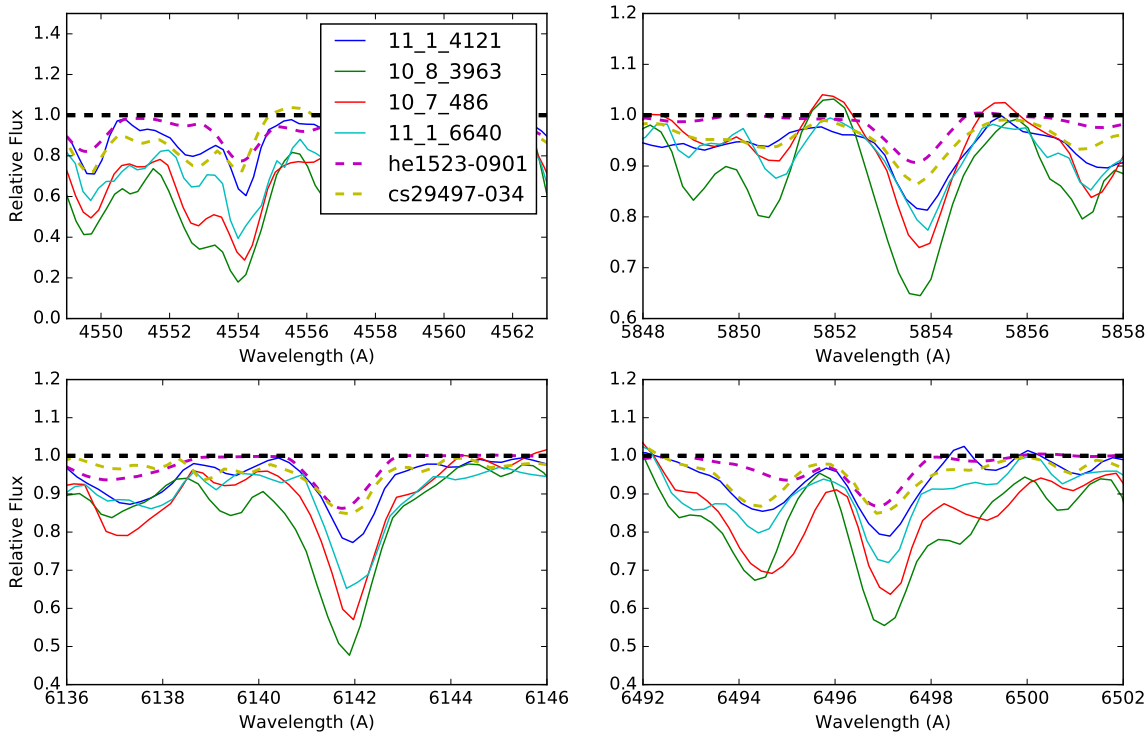

FIG. 11.— Plots of barium lines at 4554 Å, 5853 Å, 6141 Å, and 6496 Å in MagE $R \sim 6000$ spectra for 4 Sculptor CEMP stars (solid lines). The MagE ($R \sim 6000$) spectrum of CS29497-034 ([Ba/Fe] = 2.23 from Aoki et al. 2007a), a halo CEMP-r/s star, and a high-resolution MIKE spectrum of HE1523-0901 ([Ba/Fe] $\sim$ 1.1 from Frebel et al. 2007), an r-process enhanced star, smoothed to $R \sim 6000$ are over plotted for comparison.

profile. This suggests that the blending features do not significantly affect the centroid of the barium lines. In Figure 11, the barium lines of the stars are over-plotted with the resolution-degraded MIKE spectrum of the halo r-process star HE 1523−0901 (Frebel et al. 2007), which has similar stellar parameters to the four Sculptor stars. The barium features of the Sculptor stars are stronger than those in the reference stars CS29497-034 ([Ba/Fe] = 2.2) and HE 1523−0901 ([Ba/Fe] = 1.1), suggesting that they are s-process enhanced stars with [Ba/Fe] > 1.0. The centroid measurements for these stars yield high [Ba/H] values of 0.36, 0.8, −0.53, and −0.18. Taking our KP-based Fe measurements at face value, these abundances translate to [Ba/Fe] = 3.00, 3.80, 2.50, and 2.60. However, these stars show strong CH features in the vicinity of the Ca II K line in their spectra. This prevents an accurate [Fe/H] measurement (see Section 5.2). Even if the [Fe/H] values of these stars were underestimated by up to 1.5 dex, these stars would still be considered s-process rich stars due to their high barium abundance. In addition, just based on the A(C) criteria described in Yoon et al. (2016), and as shown in Figure 10, these stars could independently be classified as s-process rich stars.

5.2. *Sample bias assessment*

Our M2FS sample is composed of the most metal-poor members of Sculptor as selected from measurements of the Ca II K line in lower-resolution IMACS spectra. Our initial metallicity cut based on the IMACS data attempted to include all stars with [Fe/H] < −2.9. The majority of stars are cool red giants. There is a potential for CEMP stars to be preferentially included or excluded from the M2FS sample if their metallicity measurements are systematically biased because of strong C absorption. At face value, we expect CH absorption features to depress the continuum blueward of the Ca II K line in the lower-resolution IMACS spectra, causing a lower measurement of the equivalent width of the Ca II K line and thus a faulty selection. This would mean that carbon-rich stars may be preferentially selected into our M2FS sample because they may appear to be extremely metal poor stars.

Stars whose carbon-enhancement is driven by accretion across a binary system, such as CEMP-s, Ba-strong, and CH-strong stars, have the highest A(C) values and would thus be the most likely to be preferentially selected into our sample. Indeed, we find 4 more metal-rich CEMP-s, Ba-strong, or CH-strong stars in our M2FS sample based on follow-up observations with MagE (see Section 4.6). All of these stars were initially found to have [Fe/H]$\sim$ −3.0 based on measurements of the strength of the Ca II K line. But these stars must actually be much more metal-rich as a simple comparison of the magnesium triplet region ($\sim$ 5175Å) of these stars to that of the halo CEMP-r/s star CS29497-034 ([Fe/H] = −2.9)

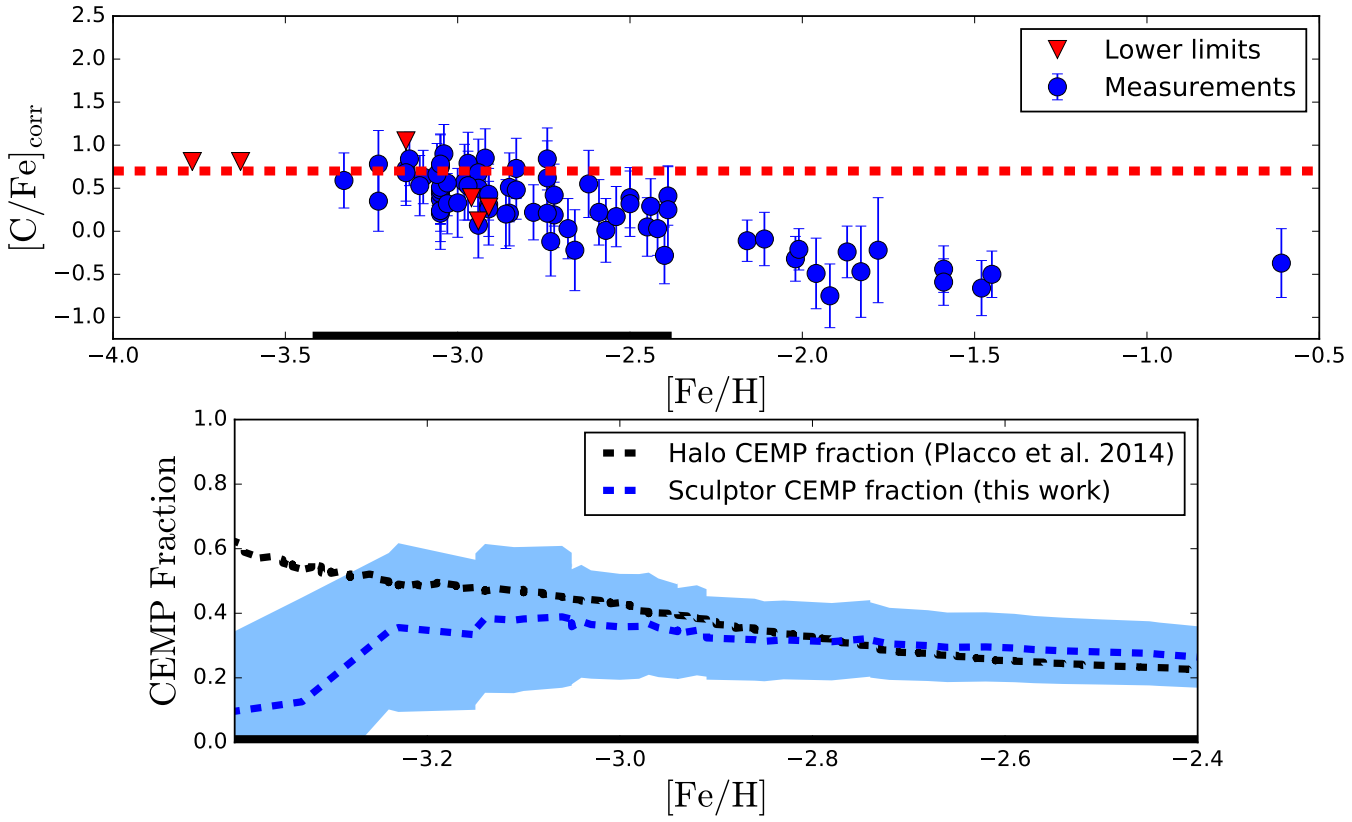

FIG. 12.— Top: [C/Fe] as a function of [Fe/H] for RGB stars in our M2FS Sculptor sample. CH strong, Ba strong, and CEMP-s candidates are not displayed in the upper panel of the plot. The displayed [C/Fe] measurements have been corrected for the evolutionary state of each star following Placco et al. (2014). The dashed red line marks the cutoff for a star to be considered a CEMP star ([C/Fe] > 0.7). Red downward-facing triangles are upper limits on [C/Fe] from non-detections of the G-band. Bottom: Measured cumulative CEMP fraction as a function of [Fe/H] for our Sculptor sample (blue) and the Milky Way halo from Placco et al. (2014) (black). The shaded blue region corresponds to the 95% confidence interval of our measured CEMP fraction.

shows (see Figure 13). Given this comparison, we also chose to investigate the magnesium triplet region of stars without extreme A(C) values to determine whether their metallicity measurements were biased.

For each star in Table 5, we derived a Mg abundance from the 5172.7 Å and 5183.6 Å lines if the S/N was sufficiently high. Then, we compared the derived [Mg/Fe] ratio of these stars to the expected [Mg/Fe] ratio for dwarf galaxy stars in their metallicity regime. We would expect to see systematically higher [Mg/Fe] values if the Ca II K based metallicities were biased lower, such as in the case of stars with high A(C) values.

We consider two examples: stars 10_7_442 and 10_8_1226 have carbon abundances close to the CEMP threshold and Mg line equivalent widths in the linear regime of the curve of growth (reduced equivalent widths $\lesssim -4.45$). For these two stars, we measure [Mg/Fe] values of 0.23 and 0.17, respectively. These [Mg/Fe] ratios are roughly at the lower end of the regime of what is expected for dwarf galaxy stars at these metallicities. This suggests that we are not strongly underestimating our [Fe/H] measurements for stars that are near the CEMP threshold.

If we include stars from Table 5 with Mg line equivalent width measurements in the non-linear regime of the curve of growth at face value and adopt the M2FS metallicities and carbon abundances when available, the average [Mg/Fe] of stars with [C/Fe] > 0.50 is 0.43. This [Mg/Fe] ratio is also in the regime of expected values. As mentioned, if the metallicities were substantially underestimated, we would expect to get much larger [Mg/Fe] values. For comparison, all the CEMP-s candidates have [Mg/Fe] $\gtrsim$ 1.0 if we take the KP-based [Fe/H] measurements at face value. While these Mg abundance estimates may have large uncertainties (up to ~ 0.4 dex, as is expected for data of this quality), they suggest we are not strongly biased in our metallicity estimates for stars without copious carbon-enhancement.

We also compared our observed MagE spectra to MIKE spectra of CS22892-52 ([Fe/H] = −3.16; $T_{\rm eff}$ = 4690 K) and HD122563 ([Fe/H] = −2.93; $T_{\rm eff}$ = 4500 K) that had been degraded to match the resolution of the MagE data. Measurements of these standard stars are from Roederer et al. (2014). We find that the strengths of the Mg b lines observed with MagE appear to be roughly consistent with what is expected from our Ca II K derived metallicities.

Thus, only stars with very strong carbon enhancement are incorrectl selected into our M2FS sample. These stars are overwhelmingly likely to have their carbon abundance elevated by accretion from a binary companion (see Figure 10), and should already be excluded in a calculation of the CEMP fraction. This confirms that our selection is not biased in favor of CEMP-no stars.

Below a fiducial metallicity of [Fe/H] ~ -3.0 and after excluding CEMP-s, Ba-strong, and CH-strong stars, we can reasonably assume that there is not a strong bias toward high carbon enhancement in our EMP sample in Sculptor.

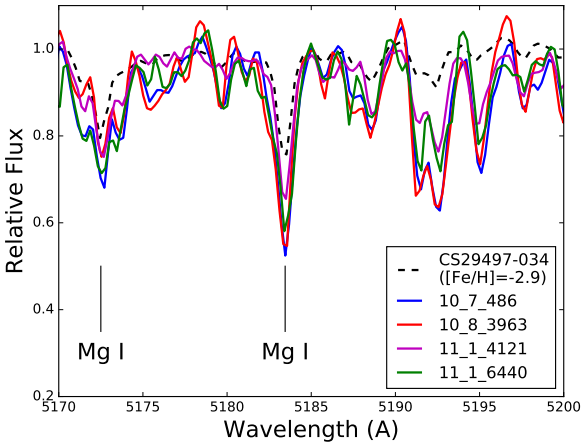

FIG. 13.— Plot of the Mg region of the MagE spectra of CS29497-034 ([Fe/H] $= -2.9$) and four other more metal-rich Sculptor members. These stars were classified as [Fe/H]~ -3.0 from measurements of the Ca II K line. It appears that the strong carbon-enhancement of these Sculptor members biased the Ca II K metallicities in lower-resolution spectra (see Section 5.2).

5.3. *Measurement of the CEMP fraction in Sculptor*

In a measurement of the CEMP fraction, we must exclude stars whose carbon enhancement is extrinsic (e.g. driven by accretion from a binary companion). We identify such stars in our M2FS sample by applying the Yoon et al. criterion (see Figure 10), as discussed in Section 4.6 and Section 5.1. We then excluded 90% of those stars, which is the probability of correct classification according to Yoon et al., from our calculation of the CEMP fraction.

We note that there is a group of stars that sits blueward of the Sculptor RGB by up to $\sim$0.25 mag (see Figure 1). Despite detailed investigation, the evolutionary status and hence the nature of these stars remains somewhat ambiguous. While they are generally bluer than would be expected for Sculptor RGB stars, they do tend to have velocities similar to Sculptor. Due to this uncertainty, we thus cautiously exclude these stars from our calculation of the CEMP fraction and we list them separately in Table 6. Since they comprise only a small portion of the sample, the CEMP fraction is largely unchanged by their exclusion.

We determined the CEMP fraction by accounting for the probability that any individual star in our sample is carbon enhanced ([C/Fe] > 0.7). We assigned a probability that each star is carbon enhanced based on its [C/Fe] measurement and assuming that the uncertainty on [C/Fe] is normally distributed. Finally, we computed a cumulative CEMP fraction for each metallicity range by finding the expected number of CEMP stars in that subset based on the probabilities of each member being carbon enhanced. We then divided the expected number of CEMP stars by the total number of stars in the subset. This approach enables us to accurately constrain the overall population of such stars even though we are not able to identify individual CEMP stars with high (p>0.95) confidence.

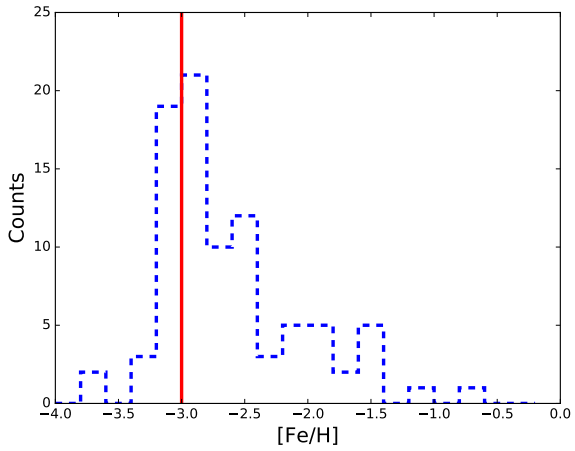

FIG. 14.— Histogram of the metallicities measured for 89 stars. Star with lower limits on metallicities are not included. The vertical red line indicates the cutoff for extremely metal-poor stars ([Fe/H]< -3.0). After excluding lower limits on [Fe/H], we detect 24 extremely metal-poor star candidates.

To derive an uncertainty on this CEMP fraction, we modeled the CEMP classification as a random walk where p_i is the probability of a given star being a CEMP star. This formulation yields an uncertainty on the CEMP fraction of $\Sigma_i \sqrt{p_i \times (1-p_i)/N}$. This uncertainty matches the uncertainty derived from Monte Carlo simulations of the CEMP fraction. We can then measure the observed cumulative CEMP fraction, and an uncertainty on the fraction, as a function of [Fe/H]. While abundance uncertainties in [C/Fe] for our sample are almost certainly non-Gaussian as the distributions of $T_{\rm eff}$ and $\log g$ residuals with respect to Kirby et al. (2013) are asymmetric, this method allows us to place a rough uncertainty on the observed CEMP fraction. The results of this analysis are shown in Figure 12. To test the impact of non-gaussianity, we compiled the individual [C/Fe] measurements that were used to calculate the uncertainty on the final carbon abundance of each star (see Section 4.2). We then calculated the fraction of those [C/Fe] measurements that were greater than 0.7 dex for stars with [Fe/H] < -3.0. We find that the fraction of those [C/Fe] measurements ($\sim 40\%$) is in agreement with our final reported CEMP fraction for EMP stars.

We measure a CEMP fraction of 0.36 ± 0.08 for stars below [Fe/H] $= -3.0$ in Sculptor. If we instead take the simpler approach of dividing the number of CEMP stars by the total number of stars after excluding 10 of the 11 probable CEMP-s stars, we derive a CEMP fraction of 0.24 (6/25) for stars below [Fe/H] $= -3.0$. The latter fraction is likely lower because our carbon abundances have large uncertainties ($\sim$ 0.35 dex) and a number of stars lie right below the cutoff of the CEMP classification. Exactly this fact has been taken into account by the method described in the previous paragraph, so we adopt the former measurement.

6. DISCUSSION AND CONCLUSION

TABLE 5
Stellar parameters and abundances from MagE spectra

Names	Slit (arcsec)	Log (g) (dex)	Teff (K)	$[Fe/H]_{KP}$ (dex)	A(C) (dex)	[C/Fe] (dex)	$[C/Fe]_{corr}$ (dex)	$[C/Fe]_{final}$ (dex)	[Ba/H] (dex)
CS29497−034†	0.7	1.50	4900	-2.90 ± 0.27	8.25 ± 0.29	2.60 ± 0.10	0.09	2.69 ± 0.10	−0.70:‡
10_8_3963	0.7	1.08	4513	> -3.00	8.10 ± 0.15	...	...	...	0.80:‡
10_7_486	0.7	1.05	4523	> -2.64	7.96 ± 0.15	...	...	...	0.36:‡
11_1_6440	0.7	1.29	4605	> -2.78	7.82 ± 0.15	...	...	...	−0.18:‡
11_1_4121	0.7	1.24	4579	> -3.03	7.52 ± 0.10	...	...	...	−0.53:‡
11_1_4422	1.0	1.75	4810	-2.85 ± 0.23	6.80 ± 0.34	1.10 ± 0.25	0.16	1.26 ± 0.25	...
6_5_1598	1.0	1.08	4516	-2.83 ± 0.16	6.02 ± 0.26	0.30 ± 0.20	0.65	0.95 ± 0.20	...
11_2_661	1.0	1.16	4550	-2.93 ± 0.17	5.67 ± 0.23	0.05 ± 0.15	0.67	0.72 ± 0.15	...
10_8_1566	1.0	1.53	4659	-2.11 ± 0.34	5.84 ± 0.40	-0.60 ± 0.20	0.47	-0.13 ± 0.20	...
7_4_2408	1.0	1.06	4524	-2.64 ± 0.16	5.51 ± 0.26	-0.40 ± 0.20	0.72	0.32 ± 0.20	...
11_1_4673	1.0	1.21	4570	-2.94 ± 0.18	5.31 ± 0.27	-0.30 ± 0.20	0.65	0.35 ± 0.20	...
10_8_3804	1.0	1.62	4752	> -2.78	8.24 ± 0.22	...	...	...	...
11_1_3334†	1.0	1.62	4721	...	7.88 ± 0.15	...	...	...	...
6_5_505†	1.0	1.57	4706	...	7.52 ± 0.15	...	...	...	...
11_2_556	1.0	2.04	4939	> -3.27	7.48 ± 0.20	...	...	...	...
7_4_3280	0.7	3.59	5518	-2.41 ± 0.25	< 6.84	< 0.70	0.00	< 0.70	...
10_8_2714	1.0	3.02	5328	-2.96 ± 0.38	< 6.59	< 1.00	0.01	< 1.01	...
10_8_3810	1.0	2.69	5199	-3.10 ± 0.33	< 6.15	< 0.70	0.01	< 0.71	...
6_5_1035	0.7	1.27	4589	-2.86 ± 0.20	5.69 ± 0.28	0.00 ± 0.20	0.61	0.61 ± 0.20	...
10_8_1226	1.0	1.47	4685	-3.05 ± 0.21	5.68 ± 0.33	0.18 ± 0.25	0.44	0.62 ± 0.25	...
10_7_442	1.0	1.61	4752	-3.33 ± 0.22	5.67 ± 0.30	0.45 ± 0.20	0.29	0.74 ± 0.20	...
7_4_1992	1.0	1.66	4769	-3.14 ± 0.22	5.60 ± 0.33	0.19 ± 0.25	0.23	0.42 ± 0.25	...
11_1_4296	1.0	1.52	4720	-3.99 ± 0.22	< 5.56	< 1.00	0.36	< 1.36	...
11_1_6015	1.0	1.87	4824	-2.42 ± 0.30	5.53 ± 0.36	-0.60 ± 0.20	0.12	-0.48 ± 0.20	...
10_7_790	0.7	1.23	4574	-3.03 ± 0.17	5.47 ± 0.34	-0.05 ± 0.30	0.63	0.58 ± 0.30	...
6_6_402	1.0	1.68	4802	-3.91 ± 0.25	< 5.44	< 0.80	0.17	< 0.97	...
10_7_923	1.0	1.39	4666	-3.87 ± 0.20	< 4.88	< 0.20	0.49	< 0.69	...

Note. — Stellar parameters and [Fe/H] for CS29497−034 are from Aoki et al. (2007a). Stars in the top portion were observed as a follow-up to M2FS observations to confirm [C/Fe] measurements, and stars in the bottom portion were observed immediately after the initial IMACS observations as EMP candidates.
†The S/N over the Ca II K feature was too low to estimate a [Fe/H] from the KP index. The M2FS [Fe/H] was assumed when calculating [C/Fe] (See Table 6)
‡The colon (:) indicates large and uncertain error bars

The overall aim of this study has been to establish the early chemical evolution of Sculptor by studying a sample of metal-poor stars in this galaxy. In particular, we obtained metallicity ([Fe/H]) and carbon abundance ([C/Fe]) measurements for 100 metal-poor stars in Sculptor using medium-resolution M2FS spectroscopy. We identify 21 carbon-enhanced metal-poor star candidates (CEMP; [C/Fe] > 0.7, [Fe/H] < -1.0), and 24 extremely metal-poor candidates (EMP; [Fe/H] < -3.0). The MDF of our sample is shown in Figure 14. Note that this sample is selected to have [Fe/H] ~ -3 and is not representative of the galaxy as a whole.

We also observed 31 stars with the MagE spectrograph of which 26 had $B - V < 1.2$. For ten, their carbon-enhanced nature was confirmed, enabling further insight into the origin of their carbon enhancement.

From these observations, we determine that many of our carbon-rich stars may be CEMP-s, CH-strong, or Ba-strong stars (see Sections 4.6 and 5.1) but such stars should be excluded in an estimate of the CEMP fraction. Excluding 90% of these stars, which is an approximation of their recovery rate, suggests a true CEMP fraction of 36% (see Section 5.3) for EMP stars in Sculptor (see Figure 12).

Prior to this study, only four CEMP stars had been identified in Sculptor (Skúladóttir et al. 2015b; Lardo et al. 2016; Salgado et al. 2016). Of those, only one was a CEMP-no star, resulting in an apparent disagreement between the CEMP fraction of Sculptor and the CEMP fraction of the Milky Way halo ($\sim 42\%$). This discrepancy, if true, would have hinted at a divergence of the earliest phases of chemical evolution, as reflected in the most metal-poor stars in the halo and in Sculptor. However, our CEMP fraction of $\sim 36\%$ for EMP stars in Sculptor is in agreement with the CEMP fraction of $\sim 42\%$ for EMP stars in the Milky Way halo, posing no such challenges.

In fact, our results show that Sculptor may have a similar cumulative CEMP fraction as the halo for stars with [Fe/H] < -3.0 (see Figure 12), using the compilation of metal-poor halo stars from Placco et al. (2014) for comparison. At face value, Figure 12 suggests that Sculptor and the halo have the same CEMP fraction at all metallicities below [Fe/H] $= -2.5$. However, the large number of stars in our sample with [Fe/H] ~ -2.8 biases the measurement of the cumulative CEMP fraction towards the value at metallicities lower than that number. Contrary to previous work, this suggests that a high CEMP star fraction may be a defining characteristic of the low metallicity Sculptor population after all, and also suggests that in Sculptor, early chemical evolution was driven by high [C/Fe] producing objects such as fallback supernovae with large [C/Fe] yields and/or massive rotating stars with large CNO yields (Limongi et al. 2003; Umeda & Nomoto 2003; Iwamoto et al. 2005; Hirschi 2007; Meynet et al. 2010; Heger & Woosley 2010; Joggerst et al. 2010; Tominaga et al. 2014).

This result indicates that the earliest stars in Sculp-

tor and, perhaps, more generally in all classical dSphs, may have undergone similar processes of early chemical enrichment as the birthplaces of halo stars did. This has already been suggested for the ultra-faint dwarf galaxies (Frebel et al. 2010b). Furthermore, because of the similar CEMP fractions, the origin of CEMP stars in the halo may also lie within early analogs of the surviving dwarf galaxies.

However, we do find that none of our CEMP stars have [C/Fe] > 1.0, whereas 32% of stars in the halo with [Fe/H] < -3.0 have [C/Fe] > 1.0 (Placco et al. 2014). This discrepancy implies that the distribution and magnitude of carbon-enhancement of CEMP stars in the halo may be different from that in Sculptor. Thus, while our result does indicate some level of similarity in early chemical enrichment among Sculptor and the Milky Way halo in terms of the CEMP fraction, there may be a level of inhomogeneity in producing the most carbon-enhanced stars. More observations of Sculptor will further confirm or refute our findings and shed more light on the enrichment history of this galaxy.

Finally, it is interesting to note that the vast majority of CEMP stars in the Milky Way halo with [Fe/H] < -3.0 are CEMP-no stars, which are stars that display no enhancement in neutron-capture elements. If our population of CEMP-s candidates have [Fe/H] < -2.90, this sample might suggest a discrepancy between the halo and Sculptor in the occurrence rate of CEMP-s stars at low metallicities. However, all of the CEMP-s candidates have only lower limits on their metallicities since strong carbon features blue-ward of the Ca II K line preclude an accurate metallicity measurement. Additional observations with higher resolution spectrographs are needed to verify whether any of our CEMP-s candidates may be EMP stars, although it is unlikely.

Given that most of our CEMP-no candidates have [Fe/H] < -2.8, the previous scarcity of CEMP stars in Sculptor can likely be explained by the overall rarity of EMP stars in Sculptor and the correspondingly small stellar samples at the lowest metallicities with available [Fe/H] and [C/Fe] measurements. The previously known sample with simultaneous [Fe/H] and [C/Fe] abundances includes 198 medium-resolution measurements from Kirby et al. (2015), 94 medium-resolution measurements from Lardo et al. (2016), and 28 stars with high-resolution measurements (Shetrone et al. 2003; Geisler et al. 2005; Frebel et al. 2010a; Tafelmeyer et al. 2010; Kirby & Cohen 2012; Starkenburg et al. 2013; Skúladóttir et al. 2015b; Jablonka et al. 2015; Simon et al. 2015). Thirteen of these stars have [Fe/H] < -2.8, one of which is potentially a CEMP-no star (Scl11_1_4296 in Simon et al. (2015)). This difference (i.e., a low CEMP fraction), is likely the result of samples that did not target EMP stars systematically as was done in our IMACS survey or potentially unaccounted for sample biases. Regardless, our sample demonstrates the existence of a substantial population of CEMP stars with [Fe/H]< -2.8 in Sculptor.

In summary, we identified EMP stars in an IMACS survey (Hansen et al. in prep) and based on M2FS follow-up observations, increased the number of known metal-poor stars in Sculptor with available [Fe/H] and [C/Fe] measurements. As a result, we provide the first meaningful sample of EMP stars from which to determine CEMP fractions to learn about early chemical enrichment and evolution. Given the similarity to the halo, perhaps all dwarf galaxies share certain properties of early chemical evolution. Follow-up spectroscopy of additional EMP candidates from our IMACS survey will likely lead to even more EMP and CEMP star discoveries in other dwarf galaxies in the future.

We thank Joshua Adams for observing and reducing most of the MagE spectra and Gary da Costa for providing access to the photometric catalog for Sculptor on which these observations were based. We would also like to thank Vinicius Placco for computing carbon corrections for this paper. A.C. and A.F. are supported by NSF CAREER grant AST- 1255160. A.C acknowledges support by the Whiteman Fellowship at MIT. J.D.S acknowledges support from AST-1108811. A.F. acknowledges partial support from the Silverman (1968) Family Career Development Professorship and PHY 08-22648; Physics Frontier Center/Joint Institute for Nuclear Astrophysics (JINA) and PHY 14-30152; and Physics Frontier Center/JINA Center for the Evolution of the Elements (JINA-CEE), awarded by the US National Science Foundation. This work made use of NASA's Astrophysics Data System Bibliographic Services. M.G.W. is supported by National Science Foundation grants AST-1313045, AST-1412999. This work has made extensive use of the astropy package (Astropy Collaboration et al. 2013).

Funding for SDSS-III has been provided by the Alfred P. Sloan Foundation, the Participating Institutions, the National Science Foundation, and the U.S. Department of Energy Office of Science. The SDSS-III web site is http://www.sdss3.org/.

SDSS-III is managed by the Astrophysical Research Consortium for the Participating Institutions of the SDSS-III Collaboration including the University of Arizona, the Brazilian Participation Group, Brookhaven National Laboratory, Carnegie Mellon University, University of Florida, the French Participation Group, the German Participation Group, Harvard University, the Instituto de Astrofisica de Canarias, the Michigan State/Notre Dame/JINA Participation Group, Johns Hopkins University, Lawrence Berkeley National Laboratory, Max Planck Institute for Astrophysics, Max Planck Institute for Extraterrestrial Physics, New Mexico State University, New York University, Ohio State University, Pennsylvania State University, University of Portsmouth, Princeton University, the Spanish Participation Group, University of Tokyo, University of Utah, Vanderbilt University, University of Virginia, University of Washington, and Yale University.

Facilities: Magellan-Clay (M2FS), Magellan-Baade (MagE, IMACS).

REFERENCES

Aaronson, M., Hodge, P. W., & Olszewski, E. W. 1983, ApJ, 267, 271

Ahn, C. P., Alexandroff, R., Allende Prieto, C., Anders, F., Anderson, S. F., Anderton, T., Andrews, B. H., Aubourg, É., Bailey, S., Bastien, F. A., & et al. 2014, ApJS, 211, 17

Alvarez, R., & Plez, B. 1998, A&A, 330, 1109
Anders, E., & Grevesse, N. 1989, Geochim. Cosmochim. Acta, 53, 197
Aoki, W., Beers, T. C., Christlieb, N., Norris, J. E., Ryan, S. G., & Tsangarides, S. 2007a, ApJ, 655, 492
—. 2007b, ApJ, 655, 492
Aoki, W., Norris, J. E., Ryan, S. G., Beers, T. C., & Ando, H. 2002, ApJ, 567, 1166
Asplund, M., Grevesse, N., Sauval, A. J., & Scott, P. 2009, ARA&A, 47, 481
Astropy Collaboration, Robitaille, T. P., Tollerud, E. J., Greenfield, P., Droettboom, M., Bray, E., Aldcroft, T., Davis, M., Ginsburg, A., Price-Whelan, A. M., Kerzendorf, W. E., Conley, A., Crighton, N., Barbary, K., Muna, D., Ferguson, H., Grollier, F., Parikh, M. M., Nair, P. H., Unther, H. M., Deil, C., Woillez, J., Conseil, S., Kramer, R., Turner, J. E. H., Singer, L., Fox, R., Weaver, B. A., Zabalza, V., Edwards, Z. I., Azalee Bostroem, K., Burke, D. J., Casey, A. R., Crawford, S. M., Dencheva, N., Ely, J., Jenness, T., Labrie, K., Lim, P. L., Pierfederici, F., Pontzen, A., Ptak, A., Refsdal, B., Servillat, M., & Streicher, O. 2013, A&A, 558, A33
Azzopardi, M., Lequeux, J., & Westerlund, B. E. 1985, A&A, 144, 388
—. 1986, A&A, 161, 232
Battaglia, G. 2007, PhD thesis, Kapteyn Astronomical Institute, University of Groningen
Battaglia, G., Helmi, A., Tolstoy, E., Irwin, M., Hill, V., & Jablonka, P. 2008, ApJ, 681, L13
Beers, T. C., & Christlieb, N. 2005, ARA&A, 43, 531
Beers, T. C., Kage, J. A., Preston, G. W., & Shectman, S. A. 1990, AJ, 100, 849
Beers, T. C., Preston, G. W., & Shectman, S. A. 1992, AJ, 103, 1987
Beers, T. C., Rossi, S., Norris, J. E., Ryan, S. G., & Shefler, T. 1999, AJ, 117, 981
Blanco, V. M., & McCarthy, M. F. 1983, AJ, 88, 1442
Bromm, V., & Larson, R. B. 2004, ARA&A, 42, 79
Brooke, J. S. A., Ram, R. S., Western, C. M., Li, G., Schwenke, D. W., & Bernath, P. F. 2014, ApJS, 210, 23
Cannon, R. D., Niss, B., & Norgaard-Nielsen, H. U. 1981, MNRAS, 196, 1P
Carney, B. W. 1996, PASP, 108, 900
Castelli, F., & Kurucz, R. L. 2004, preprint (astro-ph/0405087)
Cohen, J. G., & Huang, W. 2009, ApJ, 701, 1053
—. 2010, ApJ, 719, 931
Cohen, J. G., Shectman, S., Thompson, I., McWilliam, A., Christlieb, N., Melendez, J., Zickgraf, F.-J., Ramírez, S., & Swenson, A. 2005, ApJ, 633, L109
Coleman, M. G., Da Costa, G. S., & Bland-Hawthorn, J. 2005, AJ, 130, 1065
de Boer, T. J. L., Tolstoy, E., Hill, V., Saha, A., Olsen, K., Starkenburg, E., Lemasle, B., Irwin, M. J., & Battaglia, G. 2012, A&A, 539, A103
Dotter, A., Chaboyer, B., Jevremović, D., Kostov, V., Baron, E., & Ferguson, J. W. 2008, ApJS, 178, 89
Dressler, A., Bigelow, B., Hare, T., Sutin, B., Thompson, I., Burley, G., Epps, H., Oemler, A., Bagish, A., Birk, C., Clardy, K., Gunnels, S., Kelson, D., Shectman, S., & Osip, D. 2011, PASP, 123, 288
Eisenstein, D. J., Weinberg, D. H., Agol, E., Aihara, H., Allende Prieto, C., Anderson, S. F., Arns, J. A., Aubourg, É., Bailey, S., Balbinot, E., & et al. 2011, AJ, 142, 72
Frebel, A., Christlieb, N., Norris, J. E., Thom, C., Beers, T. C., & Rhee, J. 2007, ApJ, 660, L117
Frebel, A., Kirby, E. N., & Simon, J. D. 2010a, Nature, 464, 72
Frebel, A., & Norris, J. E. 2015, ARA&A, 53, 631
Frebel, A., Simon, J. D., Geha, M., & Willman, B. 2010b, ApJ, 708, 560
Frebel, A., Simon, J. D., & Kirby, E. N. 2014, ApJ, 786, 74
Freeman, K., & Bland-Hawthorn, J. 2002, ARA&A, 40, 487
Frogel, J. A., Blanco, V. M., Cohen, J. G., & McCarthy, M. F. 1982, ApJ, 252, 133
Geisler, D., Smith, V. V., Wallerstein, G., Gonzalez, G., & Charbonnel, C. 2005, AJ, 129, 1428
Gilmore, G., Norris, J. E., Monaco, L., Yong, D., Wyse, R. F. G., & Geisler, D. 2013, ApJ, 763, 61
Grevesse, N., & Sauval, A. J. 1998, Space Sci. Rev., 85, 161
Gustafsson, B., Edvardsson, B., Eriksson, K., Jørgensen, U. G., Nordlund, Å., & Plez, B. 2008, A&A, 486, 951
Hansen, T. T., Andersen, J., Nordström, B., Beers, T. C., Placco, V. M., Yoon, J., & Buchhave, L. A. 2016, A&A, 588, A3
Heger, A., & Woosley, S. E. 2010, ApJ, 724, 341
Hirschi, R. 2007, A&A, 461, 571
Iwamoto, N., Umeda, H., Tominaga, N., Nomoto, K., & Maeda, K. 2005, Science, 309, 451
Jablonka, P., North, P., Mashonkina, L., Hill, V., Revaz, Y., Shetrone, M., Starkenburg, E., Irwin, M., Tolstoy, E., Battaglia, G., Venn, K., Helmi, A., Primas, F., & François, P. 2015, A&A, 583, A67
Jacobson, H. R., Keller, S., Frebel, A., Casey, A. R., Asplund, M., Bessell, M. S., Da Costa, G. S., Lind, K., Marino, A. F., Norris, J. E., Peña, J. M., Schmidt, B. P., Tisserand, P., Walsh, J. M., Yong, D., & Yu, Q. 2015, ApJ, 807, 171
Ji, A. P., Frebel, A., Simon, J. D., & Geha, M. 2016, ApJ, 817, 41
Joggerst, C. C., Almgren, A., Bell, J., Heger, A., Whalen, D., & Woosley, S. E. 2010, ApJ, 709, 11
Jordi, K., Grebel, E. K., & Ammon, K. 2006, A&A, 460, 339
Jorgensen, U. G., Larsson, M., Iwamae, A., & Yu, B. 1996, A&A, 315, 204
Kelson, D. D. 2003, PASP, 115, 688
Kirby, E. N., & Cohen, J. G. 2012, AJ, 144, 168
Kirby, E. N., Cohen, J. G., Guhathakurta, P., Cheng, L., Bullock, J. S., & Gallazzi, A. 2013, ApJ, 779, 102
Kirby, E. N., Cohen, J. G., Smith, G. H., Majewski, S. R., Sohn, S. T., & Guhathakurta, P. 2011, ApJ, 727, 79
Kirby, E. N., Guhathakurta, P., Bolte, M., Sneden, C., & Geha, M. C. 2009, ApJ, 705, 328
Kirby, E. N., Guhathakurta, P., Simon, J. D., Geha, M. C., Rockosi, C. M., Sneden, C., Cohen, J. G., Sohn, S. T., Majewski, S. R., & Siegel, M. 2010, ApJS, 191, 352
Kirby, E. N., Guhathakurta, P., & Sneden, C. 2008, ApJ, 682, 1217
Kirby, E. N., Guo, M., Zhang, A. J., Deng, M., Cohen, J. G., Guhathakurta, P., Shetrone, M. D., Lee, Y. S., & Rizzi, L. 2015, ApJ, 801, 125
Koch, A., & Rich, R. M. 2014, ApJ, 794, 89
Kramida, A., Yu. Ralchenko, Reader, J., & and NIST ASD Team. 2014, NIST Atomic Spectra Database (ver. 5.2), [Online]. Available: `http://physics.nist.gov/asd` [2014, October 17]. National Institute of Standards and Technology, Gaithersburg, MD.
Kupka, F., Piskunov, N., Ryabchikova, T. A., Stempels, H. C., & Weiss, W. W. 1999, A&AS, 138, 119
Kurucz, R. L. 1992, Revista Mexicana de Astronomia y Astrofisica, 23, 45
Lai, D. K., Lee, Y. S., Bolte, M., Lucatello, S., Beers, T. C., Johnson, J. A., Sivarani, T., & Rockosi, C. M. 2011, ApJ, 738, 51
Lardo, C., Battaglia, G., Pancino, E., Romano, D., de Boer, T. J. L., Starkenburg, E., Tolstoy, E., Irwin, M. J., Jablonka, P., & Tosi, M. 2016, A&A, 585, A70
Limongi, M., Chieffi, A., & Bonifacio, P. 2003, ApJ, 594, L123
Lucatello, S., Tsangarides, S., Beers, T. C., Carretta, E., Gratton, R. G., & Ryan, S. G. 2005, ApJ, 625, 825
Marigo, P., Girardi, L., Bressan, A., Groenewegen, M. A. T., Silva, L., & Granato, G. L. 2008, A&A, 482, 883
Marshall, J. L., Burles, S., Thompson, I. B., Shectman, S. A., Bigelow, B. C., Burley, G., Birk, C., Estrada, J., Jones, P., Smith, M., Kowal, V., Castillo, J., Storts, R., & Ortiz, G. 2008, in Proc. SPIE, Vol. 7014, Ground-based and Airborne Instrumentation for Astronomy II, 701454
Masseron, T., Plez, B., Van Eck, S., Colin, R., Daoutidis, I., Godefroid, M., Coheur, P.-F., Bernath, P., Jorissen, A., & Christlieb, N. 2014, A&A, 571, A47
Mateo, M., Bailey, J. I., Crane, J., Shectman, S., Thompson, I., Roederer, I., Bigelow, B., & Gunnels, S. 2012, in Proc. SPIE, Vol. 8446, Ground-based and Airborne Instrumentation for Astronomy IV, 84464Y
McClure, R. D., & Woodsworth, A. W. 1990, ApJ, 352, 709
McWilliam, A. 1997, ARA&A, 35, 503
Meynet, G., Hirschi, R., Ekstrom, S., Maeder, A., Georgy, C., Eggenberger, P., & Chiappini, C. 2010, A&A, 521, A30

Mould, J. R., Cannon, R. D., Frogel, J. A., & Aaronson, M. 1982, ApJ, 254, 500
Norris, J. E., Gilmore, G., Wyse, R. F. G., Yong, D., & Frebel, A. 2010a, ApJ, 722, L104
Norris, J. E., Yong, D., Bessell, M. S., Christlieb, N., Asplund, M., Gilmore, G., Wyse, R. F. G., Beers, T. C., Barklem, P. S., Frebel, A., & Ryan, S. G. 2013, ApJ, 762, 28
Norris, J. E., Yong, D., Gilmore, G., & Wyse, R. F. G. 2010b, ApJ, 711, 350
Oyarzún, G. A., Blanc, G. A., González, V., Mateo, M., Bailey, III, J. I., Finkelstein, S. L., Lira, P., Crane, J. D., & Olszewski, E. W. 2016, ApJ, 821, L14
Piskunov, N. E., Kupka, F., Ryabchikova, T. A., Weiss, W. W., & Jeffery, C. S. 1995, A&AS, 112, 525
Placco, V. M., Frebel, A., Beers, T. C., & Stancliffe, R. J. 2014, ApJ, 797, 21
Plez, B. 2012, Turbospectrum: Code for spectral synthesis, Astrophysics Source Code Library
Ratnatunga, K. U., & Freeman, K. C. 1989, ApJ, 339, 126
Richer, H. B., & Westerlund, B. E. 1983, ApJ, 264, 114
Roederer, I. U., & Kirby, E. N. 2014, MNRAS, 440, 2665
Roederer, I. U., Preston, G. W., Thompson, I. B., Shectman, S. A., Sneden, C., Burley, G. S., & Kelson, D. D. 2014, AJ, 147, 136
Romano, D., & Starkenburg, E. 2013, MNRAS, 434, 471
Rossi, S., Beers, T. C., & Sneden, C. 1999, in Astronomical Society of the Pacific Conference Series, Vol. 165, The Third Stromlo Symposium: The Galactic Halo, ed. B. K. Gibson, R. S. Axelrod, & M. E. Putman, 264
Rossi, S., Beers, T. C., Sneden, C., Sevastyanenko, T., Rhee, J., & Marsteller, B. 2005, AJ, 130, 2804
Ryan, S. G. 2003, in Astronomical Society of the Pacific Conference Series, Vol. 304, CNO in the Universe, ed. C. Charbonnel, D. Schaerer, & G. Meynet, 128
Salgado, C., Da Costa, G. S., Yong, D., & Norris, J. E. 2016, MNRAS
Shetrone, M., Venn, K. A., Tolstoy, E., Primas, F., Hill, V., & Kaufer, A. 2003, AJ, 125, 684
Shetrone, M. D., Smith, G. H., Stanford, L. M., Siegel, M. H., & Bond, H. E. 2013, AJ, 145, 123
Simon, J. D., Frebel, A., McWilliam, A., Kirby, E. N., & Thompson, I. B. 2010, ApJ, 716, 446
Simon, J. D., Jacobson, H. R., Frebel, A., Thompson, I. B., Adams, J. J., & Shectman, S. A. 2015, ApJ, 802, 93
Skúladóttir, Á., Andrievsky, S. M., Tolstoy, E., Hill, V., Salvadori, S., Korotin, S. A., & Pettini, M. 2015a, A&A, 580, A129
Skúladóttir, Á., Tolstoy, E., Salvadori, S., Hill, V., & Pettini, M. 2017, A&A, 606, A71
Skúladóttir, Á., Tolstoy, E., Salvadori, S., Hill, V., Pettini, M., Shetrone, M. D., & Starkenburg, E. 2015b, A&A, 574, A129
Sneden, C., Cowan, J. J., Kobayashi, C., Pignatari, M., Lawler, J. E., Den Hartog, E. A., & Wood, M. P. 2016, ApJ, 817, 53
Sneden, C., Lawler, J. E., Cowan, J. J., Ivans, I. I., & Den Hartog, E. A. 2009, ApJS, 182, 80
Sneden, C., Lucatello, S., Ram, R. S., Brooke, J. S. A., & Bernath, P. 2014, ApJS, 214, 26
Sneden, C. A. 1973, PhD thesis, The University of Texas at Austin.
Sobeck, J. S., Kraft, R. P., Sneden, C., Preston, G. W., Cowan, J. J., Smith, G. H., Thompson, I. B., Shectman, S. A., & Burley, G. S. 2011, AJ, 141, 175
Starkenburg, E., Hill, V., Tolstoy, E., François, P., Irwin, M. J., Boschman, L., Venn, K. A., de Boer, T. J. L., Lemasle, B., Jablonka, P., Battaglia, G., Groot, P., & Kaper, L. 2013, A&A, 549, A88
Starkenburg, E., Hill, V., Tolstoy, E., González Hernández, J. I., Irwin, M., Helmi, A., Battaglia, G., Jablonka, P., Tafelmeyer, M., Shetrone, M., Venn, K., & de Boer, T. 2010, A&A, 513, A34
Susmitha, A., Koch, A., & Sivarani, T. 2017, ArXiv e-prints
Tafelmeyer, M., Jablonka, P., Hill, V., Shetrone, M., Tolstoy, E., Irwin, M. J., Battaglia, G., Helmi, A., Starkenburg, E., Venn, K. A., Abel, T., Francois, P., Kaufer, A., North, P., Primas, F., & Szeifert, T. 2010, A&A, 524, A58
Tolstoy, E., Hill, V., & Tosi, M. 2009, ARA&A, 47, 371
Tolstoy, E., Irwin, M. J., Helmi, A., Battaglia, G., Jablonka, P., Hill, V., Venn, K. A., Shetrone, M. D., Letarte, B., Cole, A. A., Primas, F., Francois, P., Arimoto, N., Sadakane, K., Kaufer, A., Szeifert, T., & Abel, T. 2004, ApJ, 617, L119
Tolstoy, E., Venn, K. A., Shetrone, M., Primas, F., Hill, V., Kaufer, A., & Szeifert, T. 2003, AJ, 125, 707
Tominaga, N., Iwamoto, N., & Nomoto, K. 2014, ApJ, 785, 98
Umeda, H., & Nomoto, K. 2003, Nature, 422, 871
Walker, M. G., Mateo, M., & Olszewski, E. W. 2009, AJ, 137, 3100
Yong, D., Roederer, I. U., Grundahl, F., Da Costa, G. S., Karakas, A. I., Norris, J. E., Aoki, W., Fishlock, C. K., Marino, A. F., Milone, A. P., & Shingles, L. J. 2014, MNRAS, 441, 3396
Yoon, J., Beers, T. C., Placco, V. M., Rasmussen, K. C., Carollo, D., He, S., Hansen, T. T., Roederer, I. U., & Zeanah, J. 2016, ApJ, 833, 20

TABLE 6
M2FS Measurements

Names	α (J2000)	δ (J2000)	Log (g) (dex)	Teff (K)	[Fe/H] (dex)	$[Fe/H]_{err}$ (dex)	[C/Fe] (dex)	$[C/Fe]_{err}$ (dex)	$[C/Fe]_{correction}$ (dex)	$[C/Fe]_{final}$ (dex)
				RGB members						
7_4_3266	00:58:38.77	−33:35:02.28	0.98	4461	−2.40	0.15	−1.07	0.33	0.79	−0.28
11_2_956	00:58:39.65	−33:55:34.76	1.02	4477	−2.16	0.18	−0.86	0.24	0.75	−0.11
7_4_3182	00:58:49.80	−33:37:19.10	1.61	4719	−3.05	0.26	0.07	0.37	0.3	0.37
11_1_6533	00:58:57.88	−33:41:50.34	1.43	4635	−2.98	0.22	0.09	0.44	0.48	0.57
11_1_6443	00:59:00.28	−33:43:14.64	1.03	4484	−2.45	0.17	−0.72	0.34	0.77	0.05
11_1_6267	00:59:04.05	−33:40:31.48	1.08	4503	−2.57	0.18	−0.74	0.37	0.75	0.01
11_1_6192	00:59:06.14	−33:44:11.39	1.37	4552	−2.02	0.22	−0.89	0.26	0.57	−0.32
7_4_2750	00:59:17.20	−33:38:06.68	1.36	4606	−3.05	0.2	−0.34	0.42	0.55	0.21
11_2_661	00:59:25.63	−33:58:21.42	1.18	4524	−3.10	0.16	−0.05	0.31	0.68	0.63
11_1_5047	00:59:26.68	−33:40:22.43	1.49	4662	−3.23	0.2	−0.01	0.35	0.36	0.35
7_4_2408	00:59:30.43	−33:36:05.23	1.07	4500	−2.68	0.16	−0.72	0.35	0.75	0.03
11_1_4824	00:59:30.49	−33:39:04.16	1.09	4508	−2.66	0.24	−0.97	0.47	0.75	−0.22
11_1_4673	00:59:33.63	−33:49:10.10	1.23	4546	−3.11	0.17	−0.11	0.35	0.64	0.53
11_1_4422	00:59:36.61	−33:40:38.51	1.76	4783	−3.04	0.25	0.74	0.34	0.16	0.90
11_1_4277	00:59:38.42	−33:40:11.57	1.81	4805	−2.94	0.25	< 0.00	...	0.12	< 0.12
11_1_4296	00:59:38.75	−33:46:14.58	1.55	4697	−3.33	0.22	0.25	0.32	0.34	0.59
11_1_4122	00:59:41.24	−33:48:03.56	1.2	4467	−2.01	0.2	−0.88	0.24	0.67	−0.21
11_1_3738	00:59:45.30	−33:43:53.83	1.79	4756	−1.92	0.35	−1.01	0.37	0.26	−0.75
11_1_3743	00:59:45.37	−33:45:34.19	1.66	4740	−2.97	0.23	0.53	0.36	0.26	0.79
11_1_3646	00:59:46.67	−33:47:19.71	1.72	4764	−3.05	0.24	0.55	0.38	0.2	0.75
11_1_3513	00:59:48.19	−33:46:50.01	1.59	4724	−2.62	0.27	0.18	0.39	0.37	0.55
11_2_425	00:59:50.64	−33:58:07.10	1.6	4715	−3.15	0.22	0.39	0.37	0.33	0.72
7_3_243	00:59:50.78	−33:31:47.06	1.25	4491	−1.48	0.27	−1.32	0.32	0.66	−0.66
11_1_3246	00:59:51.19	−33:44:51.82	1.36	4546	−1.83	0.58	−1.05	0.53	0.58	−0.47
10_8_4250	00:59:51.51	−33:44:02.67	1.29	4573	−2.73	0.22	−0.75	0.40	0.63	−0.12
7_4_1514	00:59:54.47	−33:37:53.50	1.23	4479	−1.45	0.26	−1.14	0.27	0.64	−0.50
10_8_4020	00:59:55.22	−33:42:11.34	1.4	4624	−3.05	0.21	−0.07	0.36	0.51	0.44
11_1_2583	00:59:57.59	−33:38:32.54	1.35	4539	−1.78	0.78	−0.78	0.61	0.56	−0.22
6_5_1598	00:59:59.09	−33:36:44.90	1.09	4492	−2.92	0.16	0.18	0.34	0.67	0.85
10_8_3751	00:59:59.33	−33:44:24.34	1.6	4711	−3.05	0.24	0.18	0.39	0.3	0.48
10_8_3709	00:59:59.95	−33:47:02.03	1.67	4742	−2.85	0.24	0.26	0.40	0.25	0.51
10_8_3698	01:00:00.04	−33:45:28.81	1.18	4546	−2.59	0.21	−0.47	0.38	0.69	0.22
10_7_923	01:00:01.12	−33:59:21.38	1.4	4641	−3.77	0.20	< 0.34	0.36	0.47	< 0.81
10_8_3625	01:00:01.44	−33:51:16.74	1.0	4469	−2.11	0.17	−0.84	0.31	0.75	−0.09
10_8_3520	01:00:03.27	−33:47:44.44	1.33	4591	−2.85	0.21	−0.38	0.38	0.59	0.21
10_8_3315	01:00:05.93	−33:45:56.39	0.99	4465	−2.54	0.18	−0.59	0.35	0.76	0.17
10_8_3167	01:00:07.86	−33:47:07.62	1.51	4672	−3.05	0.22	0.11	0.42	0.4	0.51
10_8_2933	01:00:11.19	−33:40:38.65	1.78	4790	−2.96	0.23	< 0.25	...	0.14	< 0.39
10_8_2927	01:00:11.30	−33:39:35.67	1.18	4527	−2.94	0.17	0.03	0.39	0.65	0.68
10_8_2908	01:00:11.72	−33:44:50.34	0.99	4451	−2.78	0.15	−0.53	0.32	0.75	0.22
10_8_2824	01:00:12.77	−33:38:53.56	1.45	4646	−3.14	0.22	0.39	0.31	0.45	0.84
10_8_2818	01:00:12.95	−33:42:03.91	1.2	4532	−2.83	0.19	−0.18	0.34	0.66	0.48
10_8_2730	01:00:14.49	−33:47:50.49	1.35	4601	−2.86	0.22	−0.37	0.40	0.57	0.20
10_8_2669	01:00:15.26	−33:45:49.87	1.83	4814	−2.94	0.23	−0.03	0.38	0.1	0.07
10_8_2647	01:00:15.67	−33:45:59.96	1.49	4680	−2.39	0.29	−0.11	0.34	0.52	0.41
10_8_2635	01:00:15.87	−33:45:01.90	1.39	4616	−3.05	0.2	−0.28	0.36	0.52	0.24
10_8_2558	01:00:17.03	−33:42:47.26	1.88	4837	−2.91	0.28	0.22	0.47	0.09	0.31
6_5_1035	01:00:19.33	−33:37:11.74	1.27	4564	−3.03	0.2	−0.30	0.35	0.62	0.32
6_5_948	01:00:22.37	−33:38:07.79	1.39	4633	−2.50	0.27	−0.18	0.35	0.57	0.39
10_8_2211	01:00:22.74	−33:51:22.84	1.18	4456	−1.59	0.25	−1.09	0.27	0.65	−0.44
10_8_2148	01:00:23.49	−33:41:46.18	1.76	4785	−2.83	0.27	0.55	0.35	0.18	0.73
10_8_2126	01:00:24.07	−33:45:54.41	1.4	4620	−2.74	0.24	0.38	0.36	0.46	0.84
10_8_2028	01:00:25.95	−33:48:40.71	1.53	4697	−2.39	0.51	−0.22	0.51	0.47	0.25
10_8_1887	01:00:28.43	−33:47:41.51	1.19	4530	−2.72	0.21	−0.26	0.36	0.68	0.42
10_8_1877	01:00:28.63	−33:46:02.64	1.49	4607	−1.87	0.26	−0.70	0.30	0.46	−0.24
10_8_1731	01:00:31.00	−33:47:12.23	1.96	4869	−2.91	0.23	< 0.25	...	0.03	< 0.28
6_5_736	01:00:31.87	−33:38:00.22	1.23	4547	−3.03	0.18	−0.07	0.38	0.63	0.56
10_8_1640	01:00:32.68	−33:41:05.05	1.8	4758	−1.59	0.26	−0.89	0.27	0.3	−0.59
10_8_1566	01:00:33.94	−33:40:08.24	1.04	4486	−2.42	0.2	−0.74	0.31	0.77	0.03
6_5_678	01:00:34.10	−33:35:08.73	1.38	4615	−2.74	0.24	0.09	0.43	0.53	0.62
10_7_570	01:00:36.41	−33:52:19.54	1.81	4805	−2.94	0.24	0.37	0.34	0.13	0.50
10_8_1463	01:00:36.46	−33:50:26.67	1.96	4871	−2.91	0.27	0.22	0.32	0.04	0.26
10_8_1325	01:00:39.72	−33:39:12.42	2.03	4870	−1.96	0.48	−0.53	0.41	0.04	−0.49
10_8_1308	01:00:40.35	−33:44:14.23	1.36	4603	−2.97	0.23	−0.01	0.40	0.54	0.53
10_8_1124	01:00:46.21	−33:42:34.03	1.21	4539	−2.72	0.2	−0.49	0.38	0.68	0.19
10_8_1072	01:00:47.83	−33:41:03.17	1.3	4581	−3.63	0.21	< 0.25	...	0.56	< 0.81
10_8_1062	01:00:48.14	−33:42:13.32	1.93	4859	−2.91	0.23	0.37	0.30	0.06	0.43
10_7_442	01:00:50.35	−33:52:15.67	1.62	4723	−3.15	0.22	0.39	0.38	0.29	0.68
6_5_420	01:00:51.64	−33:36:56.74	2.5	4565	−0.61	0.46	−0.40	0.40	0.03	−0.37
10_8_798	01:00:56.41	−33:49:47.18	1.37	4609	−2.74	0.23	−0.34	0.37	0.55	0.21
10_8_758	01:00:57.56	−33:39:39.74	1.64	4746	−2.50	0.28	0.00	0.38	0.32	0.32
10_8_577	01:01:06.92	−33:46:13.15	1.74	4773	−3.23	0.27	0.61	0.39	0.17	0.78

TABLE 6
M2FS Measurements

6_5_239	01:01:10.27	−33:38:37.81	1.09	4505	−2.44	0.23	−0.43	0.32	0.72	0.29
10_8_462	01:01:13.19	−33:43:20.56	1.53	4681	−3.06	0.22	0.28	0.36	0.38	0.66
10_8_320	01:01:22.24	−33:46:21.81	1.1	4493	−3.00	0.15	−0.39	0.40	0.72	0.33
10_8_265	01:01:27.22	−33:45:15.31	1.51	4671	−3.05	0.22	0.37	0.34	0.41	0.78
10_8_61	01:01:47.52	−33:47:27.64	1.6	4713	−3.15	0.25	< 0.75	...	0.3	< 1.05
					CEMP-s candidates					
11_1_6440†	00:59:00.13	−33:38:50.96	1.3	4579	> −3.04	...	...	...	...	...
11_1_5437†	00:59:19.87	−33:38:56.77	1.12	4517	> −3.41	...	...	...	...	...
11_1_4121†	00:59:41.05	−33:45:25.28	1.25	4554	> −3.12	...	...	...	...	...
11_1_3334†	00:59:49.62	−33:40:41.78	1.62	4721	> −3.24	...	...	...	...	...
10_8_3963†	00:59:56.17	−33:43:04.89	1.09	4488	> −3.09	...	...	...	...	...
10_8_3926†	00:59:56.73	−33:39:37.54	1.36	4626	> −3.76	...	...	...	...	...
10_8_3804†	00:59:58.91	−33:50:53.61	1.63	4727	> −3.15	...	...	...	...	...
10_8_2134†	01:00:23.71	−33:40:20.40	1.41	4628	> −2.98	...	...	...	...	...
10_7_486†	01:00:45.41	−33:52:14.68	1.14	4509	> −3.02	...	...	...	...	...
6_5_505†	01:00:45.76	−33:38:34.83	1.57	4706	> −3.33	...	...	...	...	...
10_8_437†	01:01:15.05	−33:50:02.63	1.24	4553	> −3.20	...	...	...	...	...
					Blueward of RGB					
10_8_4247	00:59:51.56	−33:45:07.76	3.32	5419	−2.84	0.39	< 0.40	...	0.0	< 0.40
10_8_4014	00:59:55.48	−33:45:51.48	2.88	5244	−2.99	0.42	0.64	0.51	0.01	0.65
10_8_3723	00:59:59.92	−33:51:11.79	2.96	5286	−2.38	0.82	< 0.40	...	0.01	< 0.41
10_8_3558	01:00:02.65	−33:49:18.73	3.02	5309	−2.48	0.31	< 0.4	...	0.01	< 0.41
10_8_3188	01:00:07.66	−33:49:46.99	3.32	5394	−1.98	0.45	< 0.00	...	0.0	< 0.00
10_8_3111	01:00:08.86	−33:49:49.67	2.65	5066	−1.15	0.37	−0.86	0.30	0.02	−0.84
10_8_3045	01:00:09.72	−33:47:00.79	2.49	5100	−2.55	0.28	0.16	0.39	0.01	0.17
10_8_1615	01:00:33.05	−33:43:02.26	2.61	5151	−2.55	0.34	< 0.25	...	0.01	< 0.26
10_8_1366	01:00:38.71	−33:43:16.58	2.81	5227	−2.10	0.38	−0.22	0.41	0.01	−0.21
10_8_440	01:01:14.29	−33:39:27.82	3.59	5493	−1.65	0.2	−0.45	0.31	0.0	−0.45
10_8_436	01:01:14.95	−33:47:21.34	3.35	5404	−1.42	0.83	−0.47	0.57	0.0	−0.47
6_5_163	01:01:19.89	−33:35:57.44	2.41	5055	−2.95	0.45	0.84	0.48	0.01	0.85

Note. — Stars in the upper section lie on the RGB of Sculptor, and stars in the lower section lie blueward of the RGB (see Figure 1).
† These stars are classified as likely CH-strong, Ba-strong, or CEMP-s stars due to the presence of saturated carbon features (see Sections 4.6 and 5.1).